PL-TR-92-3054

AD-A267 277

# HIGH POWER STEADY STATE MPD THRUSTERS

Monika Auweter-Kurtz
Harald Habiger
Helmut Kurtz
Herbert Schrade
Christian Sleziona
Thomas Wegmann

Institut Für Raumfahrtsysteme
Universität Stuttgart

April 1993

**DTIC**
**S** ELECTE
JUL 27 1993
**A** **D**

Final Report

93-16878

**PHILLIPS LABORATORY**
**Propulsion Directorate**
**AIR FORCE MATERIEL COMMAND**
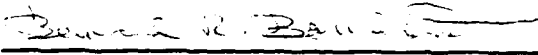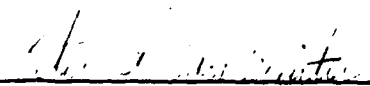**EDWARDS AIR FORCE BASE CA 93524-7001**

## NOTICE

When U.S. Government drawings, specifications, or other data are used for any purpose other than a definitely related Government procurement operation, the fact that the Government may have formulated, furnished, or in any way supplied the said drawings, specifications, or other data, is not to be regarded by implication or otherwise, or in any way licensing the holder or any other person or corporation, or conveying any rights or permission to manufacture, use or sell any patented invention that may be related thereto.

## FOREWORD

This report was prepared by the Institut für Raumfahrtsysteme, Universität Stuttgart under Grant AFOSR−89−0535, for Operating Location AC, Phillips Laboratory, Edwards AFB, CA. 93524−7001. Project Manager for Phillips Laboratory was Matt Jones.

This report has been reviewed and is approved for release and distribution in accordance with the distribution statement on the cover and on the SF Form 298.

J. MATHEW JONES
Project Manager

BERNARD R. BORNHORST
Chief, Space Propulsion Branch

PETER A. VAN SPLINTER
Director,
Applications Engineering Division

RANNEY G. ADAMS
Public Affairs Director

| REPORT DOCUMENTATION PAGE | Form Approved OMB No 0704-0188 |
|---|---|

| 1. AGENCY USE ONLY (LEAVE BLANK) | 2. REPORT DATE April 1993 | 3. REPORT TYPE AND DTAES COVERED Final  September 1989 – August 1991 |
|---|---|---|

**4. TITLE AND SUBTITLE**

**High Power Steady State MPD Thrusters**

**5. FUNDING NUMBERS**
C:   Grant AFOSR-89-0535
PE:   62302F
PR:   3058
TA:   00C4

**6. AUTHOR(S)**

Monika Auweter-Kurtz;  Harald Habiger;  Helmut Kurtz
Herbert Schrade;  Christian Sleziona;  Thomas Wegmann

**7. PERFORMING ORGANIZATION NAME(S) AND ADDRESS(FS)**

Institut FÜr Raumfahrtsysteme
Universität Stuttgart

**8. PERFORMING ORGANIZATION REPORT NUMBER**

**9. SPONSORING/MONITORING AGENCY NAME(S) AND ADDRESS(ES)**

Phillips Laboratory
OLAC-PL/RKAS
Edwards AFB, California  93524-7160

**10. SPONSORING/MONITORING AGENCY REPORT NUMBER**

**PL-TR-92-3054**

**11. SUPPLEMENTARY NOTES**

COSATI CODE(S):   22/08; 22/09

**12a. DISTRIBUTION/AVAILABILITY STATEMENT**

" Approved For Public Release; Distribution is Unlimited"

**12b. DISTRIBUTION CODE**

**13. ABSTRACT (MAXIMUM 200 WORDS)**

At the Institut fÜr Raumfahrtsysteme (IRS) rotation symmetric magneto plasma dynamic thrusters with self induced magnetic fields are investigated at high current levels in a steady state operation mode. MPD thrusters with different geometrics were compared and the influence of mass flow rate and power input on the operating conditions of the thrusters explored. By optical and probe measurements a systematic investigation of the plasma plume has been started. The investigation of the various instabilities of the arc and the plasma flow appearing at high power levels was continued. The computer code development for the geometry optimization of continous self-field MPD thrusters, running with argon, was modified by considering higher degrees of ionization, which showed better agreement with the experiement.

**14. SUBJECT TERMS**

Electric Propulsion; MPD Propulsion; Plasma Diagnostic; Instability Investigation
Flow Discharge Calculation.

**15. NUMBER OF PAGES**

**16. PRICE CODE**

| 17. SECURITY CLASSIFICATION OF REPORT Unclassified | 18. SECURITY CLASSIFICATION OF THIS PAGE Unclassified | 19. SECURITY CLASSIFICATION OF ABSTRACT Unclassified | 20. LIMITATION OF ABSTRACT SAR |
|---|---|---|---|

## Table of Contents

## List of Figures

## List of Tables

# 1. Introduction

Since the early eighties, self−field MPD−thrusters in the 100kW up to the 1 MW power range were investigated at the IRS in a steady state operation mode [1, 2, 3]. With the beginning of space exploration missions involving human passengers and with the design and construction of space stations and other large space vehicles having relatively large on board electric power supplies, possibly of up to several MW in the next decade, plasma propulsion systems have been found to be more advantageous than chemical propulsion systems, due to their higher specific impulse rates. As a result of their less complex design features and higher thrust to area ratios MPD−thrusters bear an advantage over ion thrusters.

In recent mission analyses [4, 5], the parameters for different missions were examined and it was shown that efficiencies of $\eta > 0.25$ were useful. At the same efficiency values the specific impulse $I_{sp}$ showed a secondary impact on the mission performances. For low Earth−orbital cargo missions specific impulses higher than 2000 s were suitable, while for Mars missions $I_{sp} > 4000$ s would be necessary. Therefore MPD−thrusters have to be developed, which fulfill necessary requirements and which can operate in a steady state mode. The benefits of these thrusters versus pulsed ones are the ruggedness and simplicity of power and propellant conditioning, and the more than 3 orders of magnitude smaller cathode erosion. But only when the requirements can be reached in the next few years, there will be a chance for missions, operated with MPD−thrusters.

The objective of these contracts is to try and raise the operating and testing limits of the steady state MPD−thrusters up to about 1 MW and to investigate the encountered problems; which also have a fundamental importance in regard to future planned development of MPD−thrusters in the MMW power level. Here not only the performance parameters are of interest, but also the investigation of electrode effects, instabilities and lifetime limitations. This contract grant AFSOR−89−0535 is a continuation of the former grants: AFOSR−88−0325 [6]; AFOSR−84−0394 [7]; AFOSR F49 620−82−C−100 AND ONR−N00014−G−0119 [8]; which dealt with lower power steady state MPD−thruster development.

This report describes, in sections 2 and 3, the experimental investigation and results with high power steady state nozzle types and cylindrical MPD−thrusters. The influence of geometry and propellant mass flow rates on the thruster performance data are also presented. Section 4 deals with the plasma plume diagnostics of the nozzle type MPD−thrusters, using both probe measurements and optical diagnostics. The investigation of plasma instabilities is a main research topic at the IRS, these experimental results are described in section 5. A new explanation of the so−called "Onset−Phenomenon" based on the run−away Joule heating effect was developed under grant AFOSR−91−0118 and was presented in detail in a recent Final Report [9]. Finally in section 6, some improvements to the computer codes will be explained, paying special attention to the MPD−thruster calculations when considering high levels of ionization and comparison of the numerical results with experimental ones.

## 2. Experimental results of the nozzle type MPD—thruster performance

The experimental investigations of the nozzle type MPD—thrusters with different geometries were enhanced by a new nozzle type MPD—thruster design. In Figure 2.1, the configuration of the present thrusters are compared, Figure 2.2 shows the new DT6—thruster in detail.

Throat length: 17.6 mm

propellant

anode

Throat Diameter (mm)

DT2 — ⌀24
DT5 — ⌀30
DT6 — ⌀36

arc chamber

cathode

watercooled, neutral segments

insulation
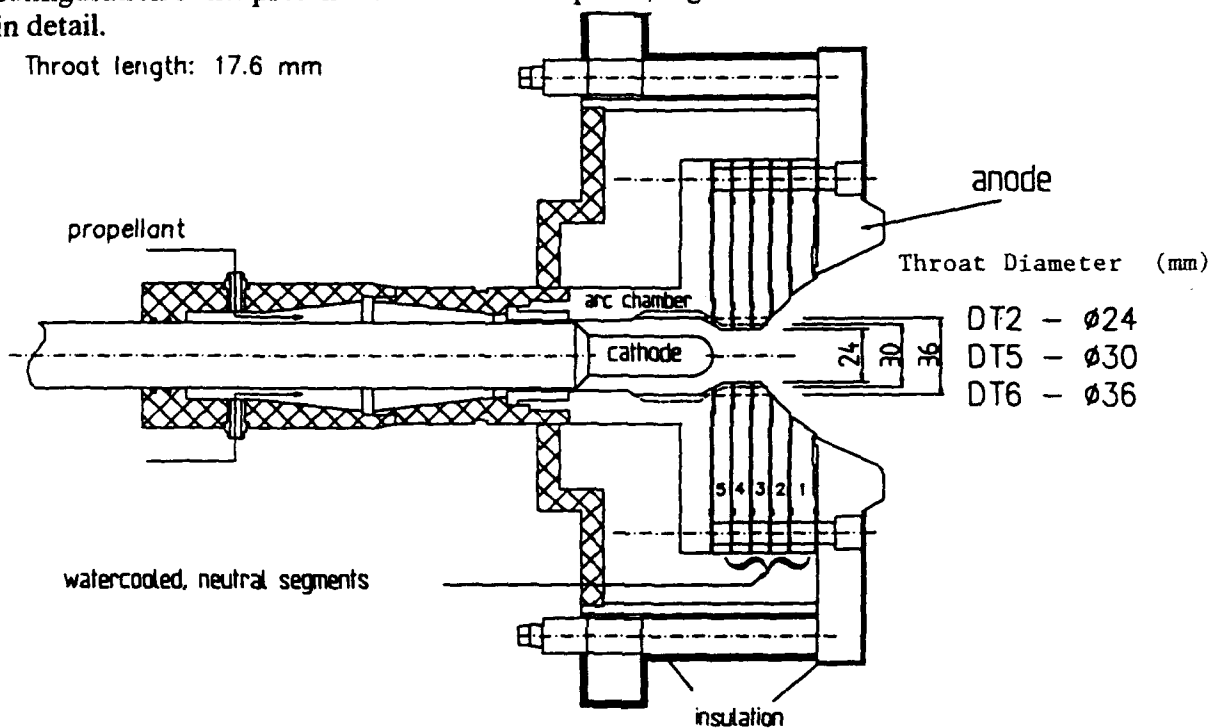
**Fig. 2.1: Configuration of the DT-thruster-head series at the IRS**

Throat Diameter:   36 mm

Gas--inlet

Anode

Arc-chamber

Cathode

watercooled, neutral segments

insulation
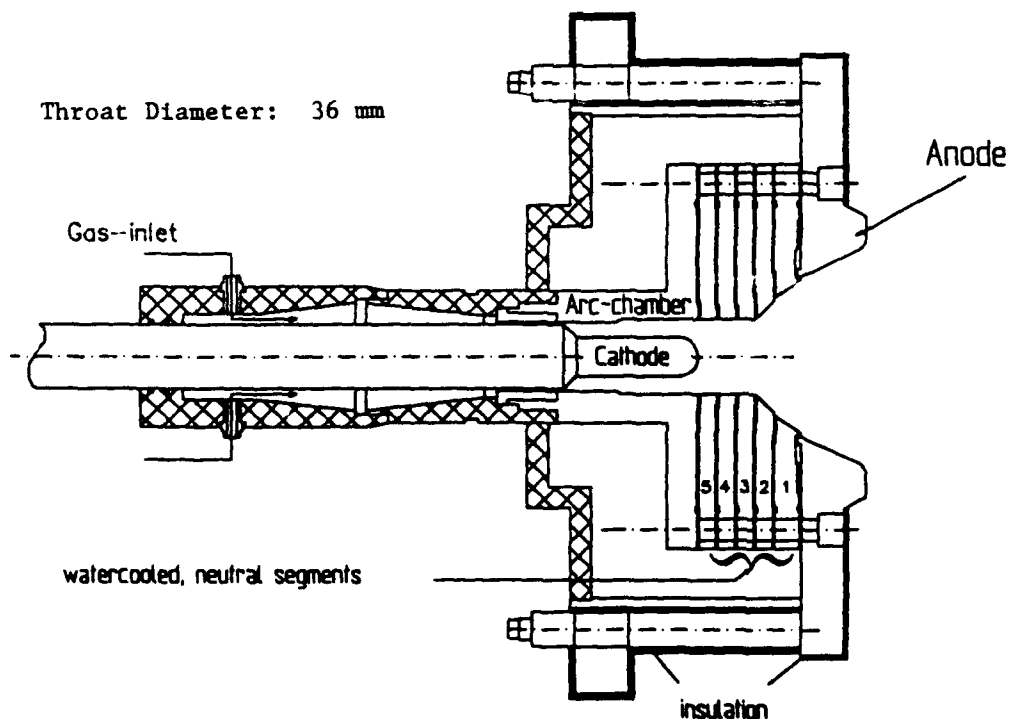
**Fig. 2.2: Configuration of the nozzle type MPD-thruster DT6**

All nozzle type thrusters are composed of an anode, a cathode, the arc chamber, and five neutral segments, which form the different throat geometries. The cathode is made of a 2% thoriated tungsten rod, while the anode and other thruster parts are tooled copper segments, which are individually cooled by high−pressure water. The different versions of the DT−thruster series differ solely in the nozzle throat diameter. Based on the heat load measurement the size of the throat area was enlarged to facilitate increased power levels, dependent on the current level capabilities of the test cathode diameter chosen. Therefore the DT2−thruster has a throat diameter of 24 mm, the DT5−thruster has a diameter of 30 mm.. For the latest MPD−thruster DT6 the three throat segments were enlarged to 36 mm and now have the same diameter as the arc chamber, so this thruster, no longer has any constriction. All other thruster parameters are identical. The outer anode diameter is 142 mm, the anode parts with greater diameter are covered with a ceramic insulation, so that the anode attachment region of the arc is relatively well bounded. The cathode, which is cast in a water−cooled copper rod, is positioned upstream of the nozzle in the so−called arc chamber. In special test series of former research periods [6], the cathode position of 85 mm, measured from the anode exit plane to the cathode tip, has proven to be an optimum value. The cathode diameter depends on throat diameter and power level. While for the DT2−thruster, a cathode of 18 mm diameter was used, the cathode diameter was enlarged for the DT6−thruster and high power levels to 24 mm, to prevent a cathode melting at high current densities.

The propellant is injected in the arc chamber, tangentially to the cathode. In contrast to former test series, in the last test period, no additional gas was injected at the anode segment. The stabilization of the discharge and the arc seems only to depend on the quality of symmetry.

The nozzle type MPD−thrusters are mounted on a thrust balance, which is installed in a vacuum tank. This tank has a length of 5 m, a diameter of 2 m, and has double water−cooled walls. For the optical diagnostics, the vacuum tank has windows with optical glasses on its side.
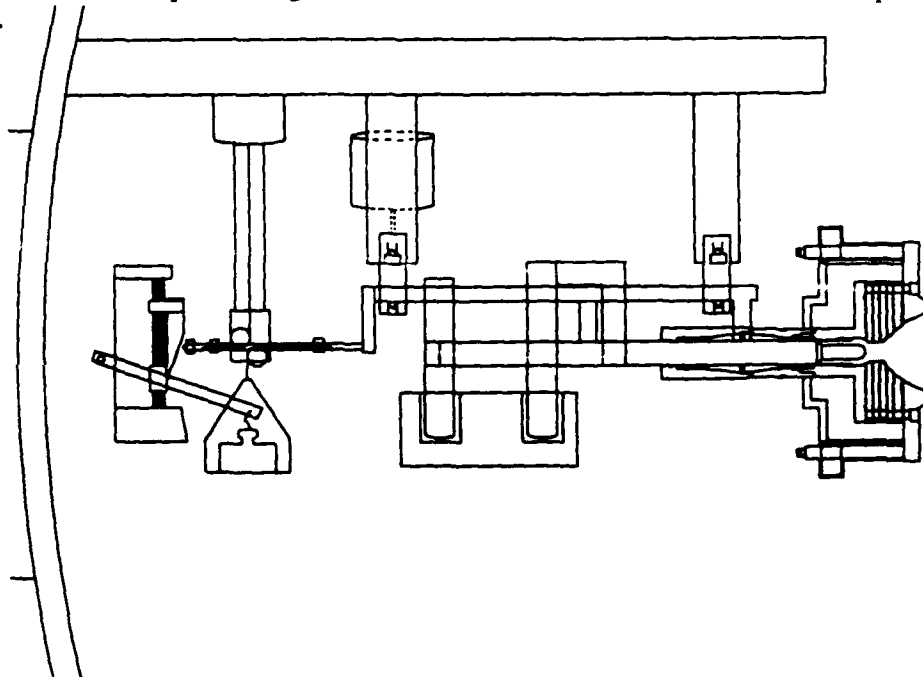


**Fig. 2.3: Scheme of the thrust balance**

The thrust balance (Fig. 2.3 ) is a pendulum thrust balance which is positioned on knife—edges, the resulting force is measured by a wire strain gauge force transducer. The current feed to the balance is achieved through mercury baths. Through nylon hoses, which form large bow in vertical planes, the cooling water and propellant are supplied to the thruster and the thrust balance. In order to eliminate errors due to electromagnetic and mechanical interactions, calibration measurements have been performed with the thruster short circuited and with running cooling water. Additionally the thrust balance is remotely calibrated before and after each test, allowing thrust measurements within an error of less than 2%. Further the current and discharge voltage, the propellant mass flow rate, the discharge chamber pressure and the thermal losses of the electrodes and each thruster segment are individually measured.

Figure 2.4 shows the data acquisition and control system, consisting of a multichannel Intercole Spectra data acquisition system controlled by a PDP 11/73, which also controls the gas valves and mass flow controllers.
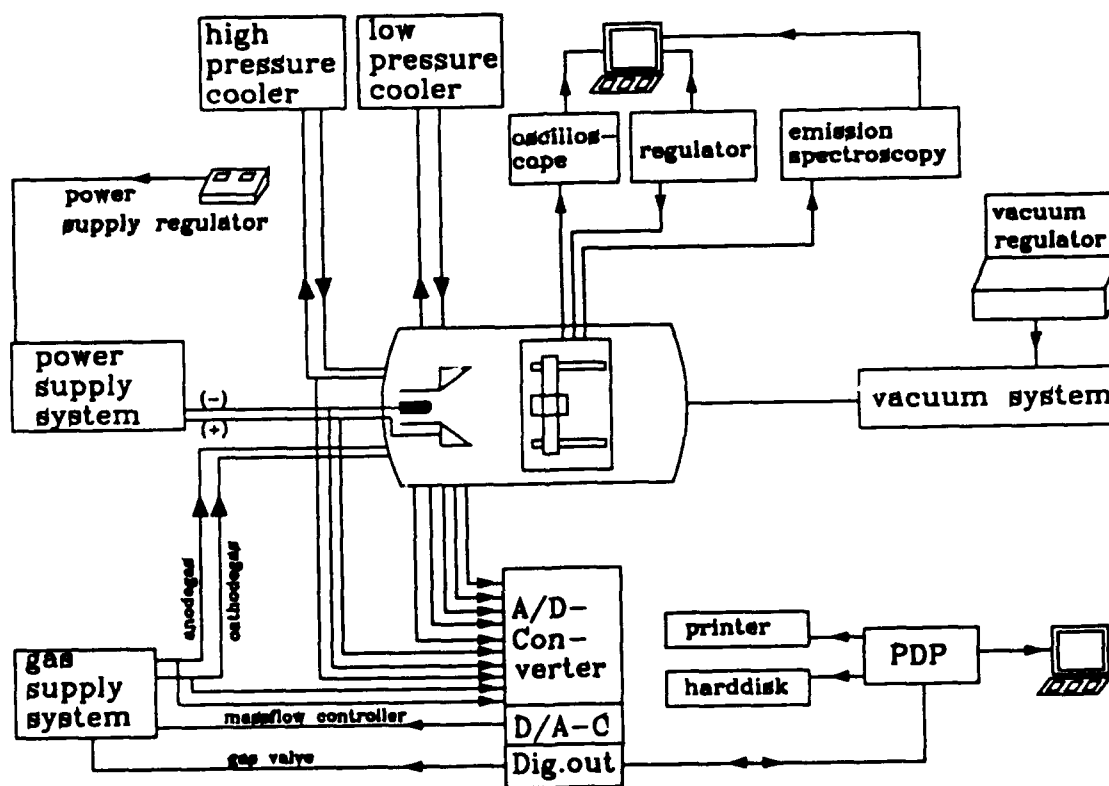
Fig. 2.4: Scheme of the supply and data measuring arrangement

In this test period, all tests have been carried out with argon as propellant, the mass flow rates were mainly set to 0.8 g/s and to 1.6 g/s in order to have a comparable standard both with former tests and with numerical results.

In Figures 2.5 and 2.6, the voltages versus current characteristics for these mass flow rates and for all three nozzle type thrusters, DT2, DT5, and DT6 are compared.

4
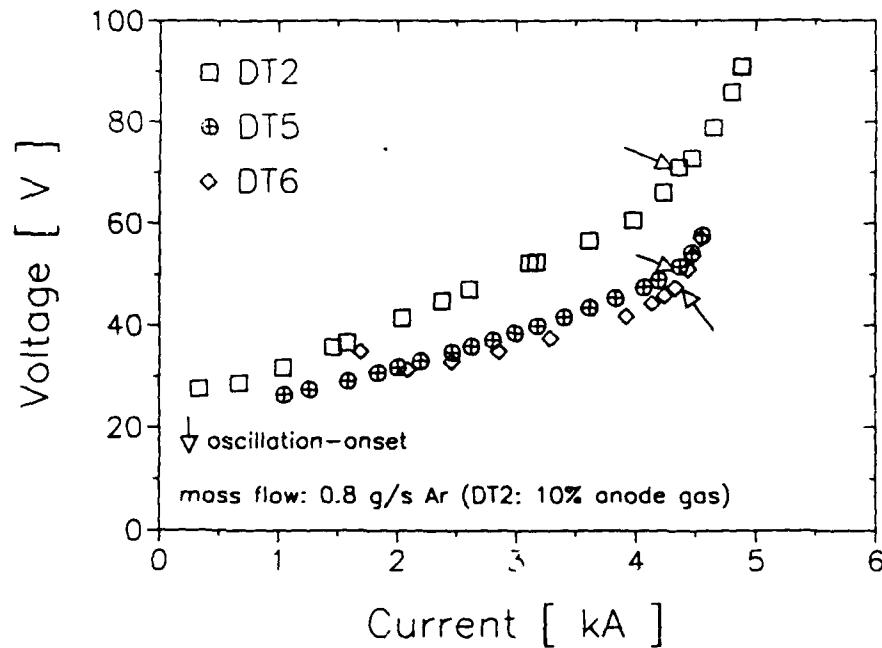
**Fig. 2.5:** Voltage vs. current curves for a mass flow rate of 0.8 g/s argon
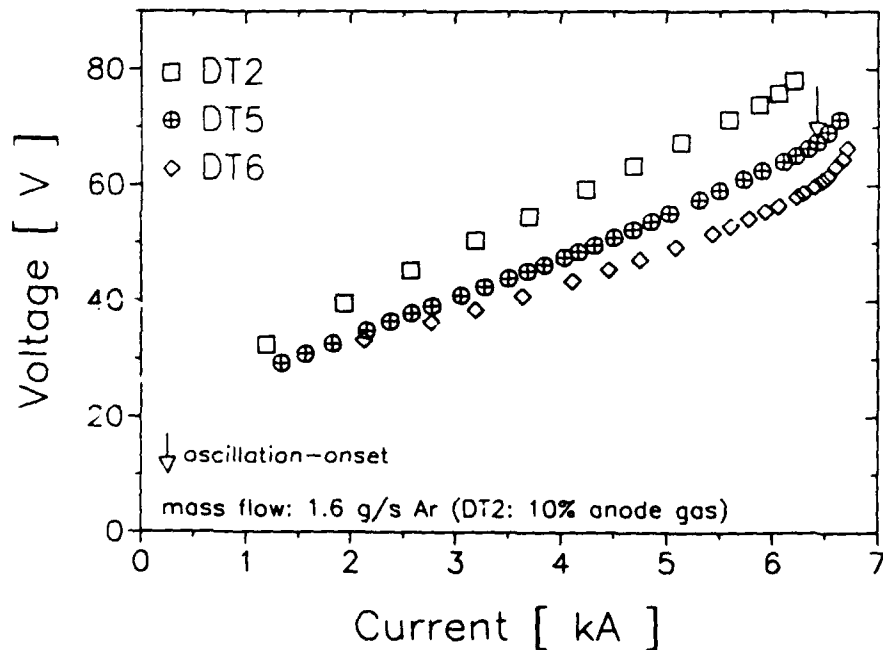


**Fig. 2.6:** Voltage vs. current curve for a mass flow rate of 1.6 g/s argon

The diagrams show that for the DT-thrusters with larger throat diameter the absolute values and also the increments of the voltage-current curves are lower. The arrows in the diagrams mark the critical current values, where strong oscillations can be detected with an antenna, indicating the beginning of the unstable operation mode of the MPD-thrusters. At the same time the voltage-current curves increase drastically. From the measurements with a mass flow rate of 0.8 g/s argon ( Fig. 2.5 ) one has to say that no strong dependence of the critical current from the thruster geometry is noticeable.

5

To the following measurements we have to give a previous explanation: the thrust performance data of the **DT6**-thruster are preliminary results, which have to be verified in future test series, especially because of the unexpected results. Unfortunately the standard thruster DT2-IRS was damaged beyond repair during a test near onset conditions, so that a once more comparable thrust measurement was not possible. Therefore one cannot fully exclude an incorrectness of the thrust balance or the measurement system. The results have not been published up to now and although they are presented here, they have to be considered with caution. We will only present them in the following diagrams without commentary.

In Figure 2.7 and 2.8 the thrust and the thrust efficiency versus current curves of the nozzle type DT-thrusters, operated with 1.6 g/s argon, are presented.
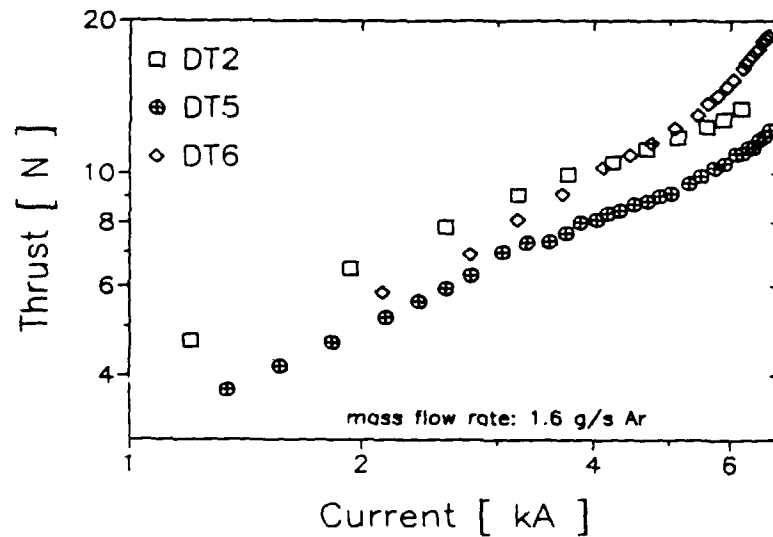


Fig. 2.7: Thrust vs. current curve of the nozzle type DT-Thrusters, running with 1.6 g/s argon. ( DT6 data are preliminary )
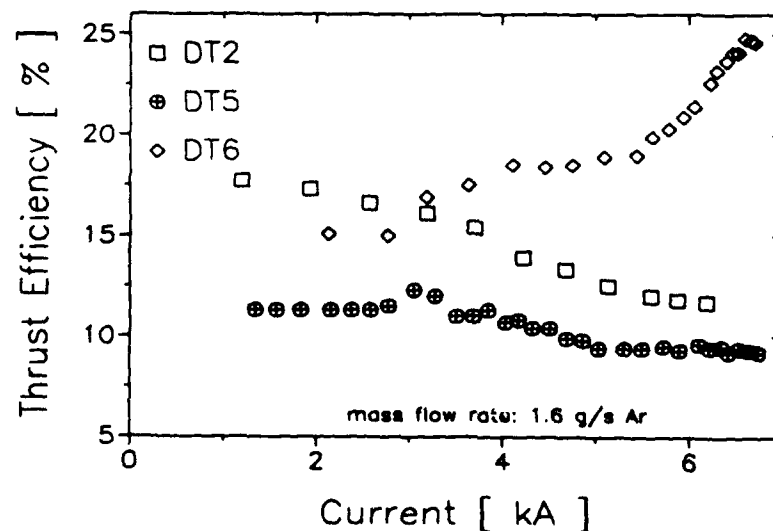


Fig. 2.8: Thrust efficiency vs. current curve of the nozzle type DT-thrusters, running with 1.6 g/s argon. ( DT6 data are preliminary )

6

At lower current levels I, the thrust T increases almost linearly with the current and at higher currents the slope of the thrust curve slowly increases. While the thrust efficiency $\eta_T$, calculated as :

$$\eta_T = \frac{T^2}{2\, m\, U\, I}$$

for the DT6-thruster increases with higher current, for the other thrusters the efficiency slowly decreases.

In the following four diagrams the results of the thermal loss measurements are presented ( Figures 2.9-2.12).
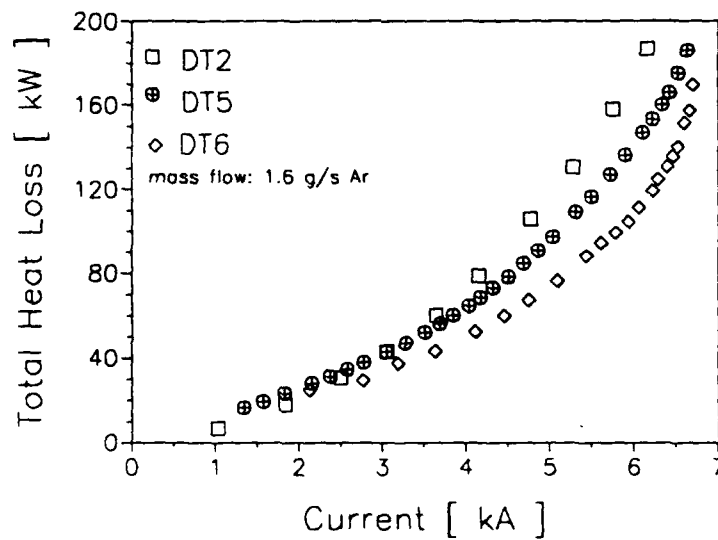


Fig. 2.9: Total Heat Loss  vs. current for the DT-thrusters, running with 1.6 g/s argon
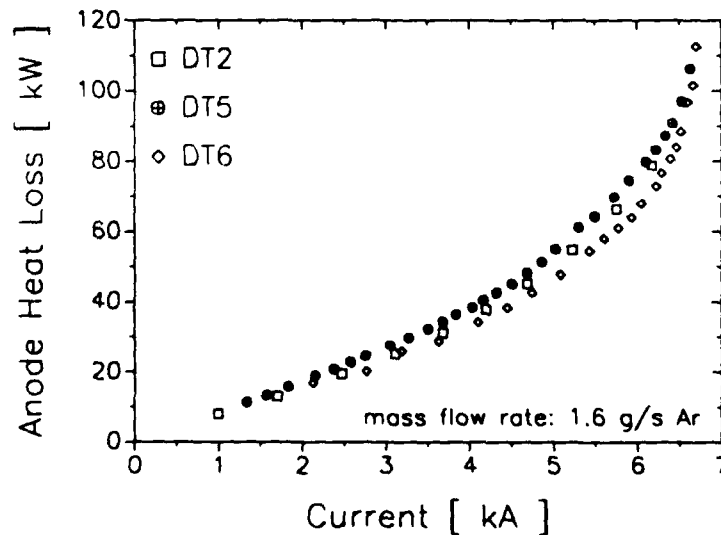


Fig. 2.10: Anode Heat Loss vs. current for the DT-thrusters, running with 1.6 g/s argon
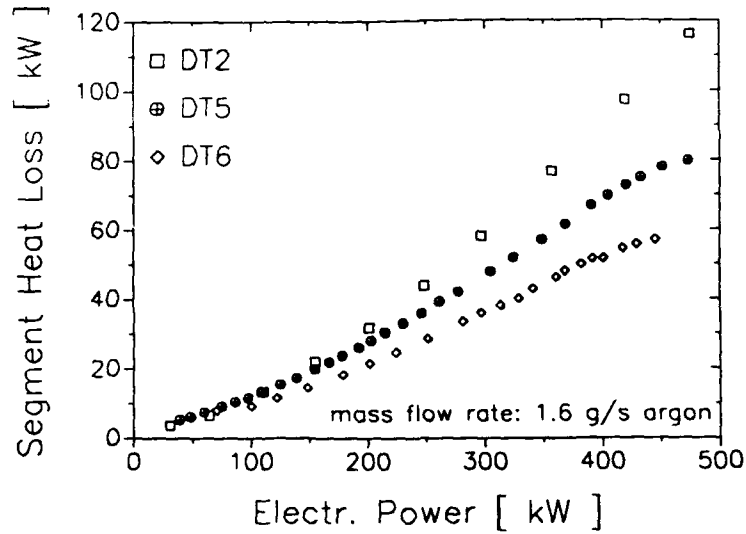
Fig. 2.11: Segment Heat Loss vs. electric power input for the DT-thrusters, running with 1.6 g/s argon
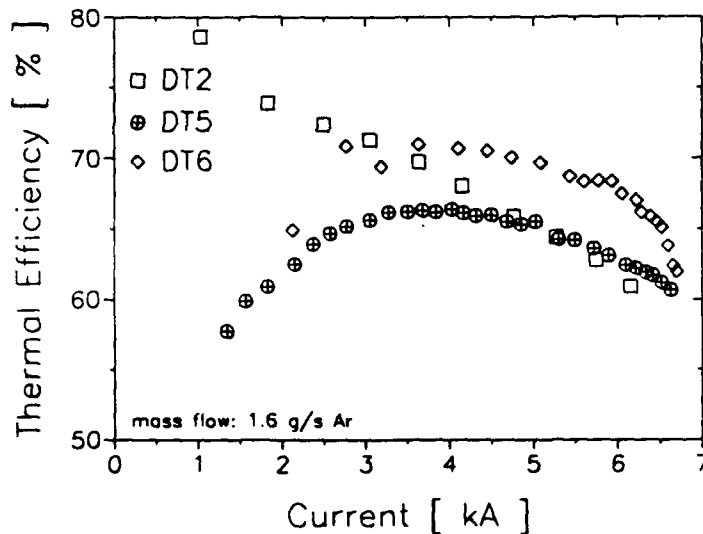


Fig. 2.12: Thermal Efficiency vs. current for the DT-thrusters, running with 1.6 g/s argon

With enlarged throat the total heat losses of the DT-thrusters decrease ( Fig. 2.9 ), mainly because of the reduced thermal losses in the throat segments ( Fig. 2.11 ). The anode heat losses are nearly independent from the geometry ( Fig. 2.10 ), drastically increasing at high current levels near onset conditions. This severe increasing of the anode loss factor is almost exclusively due to an increasing anode fall voltage $U_A$, which will be discussed in chapter 5.

The thermal efficiency $\eta_{Th}$ of the DT-thrusters are between 60% and 70% and decrease near the onset conditions because of the increasing anode fall voltage. In the other current ranges, the thermal efficiency of the DT6-thruster is in the average 5% higher than that of the other DT-thrusters, due to the lower nozzle segment losses.

In the Figures 2.13 - 2.15 the performance data of the DT2 and DT6-thruster depending on current I and mass flow variations are shown. The arrows in Figure 2.13 mark again the critical current values, where the oscillations occur. Also plotted in Figure 2.14 is

8

the electromagnetic thrust $T_m$, which was calculated with the known thrust formula of Maecker [10]:

$$T_m = \frac{\mu_0}{4\pi} I^2 \left( \ln \frac{r_a}{r_c} + \frac{3}{4} \right)$$

$T_{m,max}$ and $T_{m, min}$ are the calculated electromagnetic thrust for maximal and minimal possible anode radius $r_a$ and cathode radius $r_c$ respectively. The thrust efficiencies are displayed as a function of specific impulse in Figure 2.15.
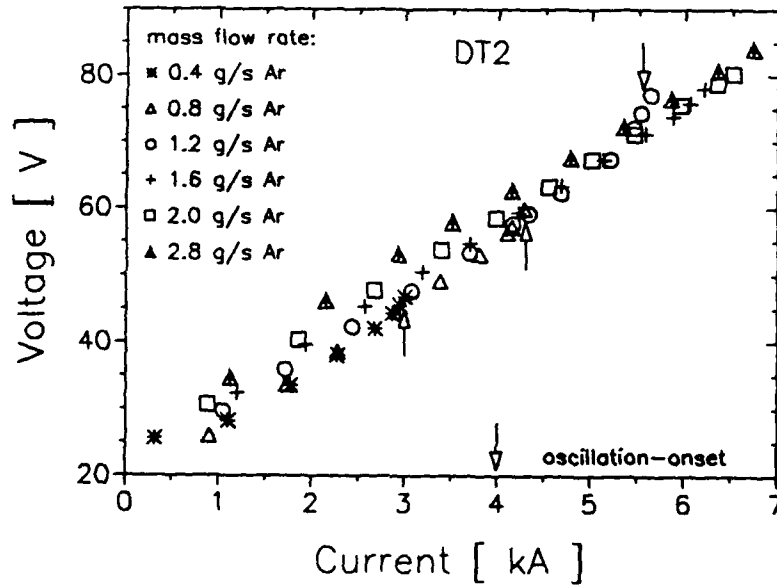


Fig. 2.13a: Voltage vs. current curves for the DT2-thruster at various mass flow rates
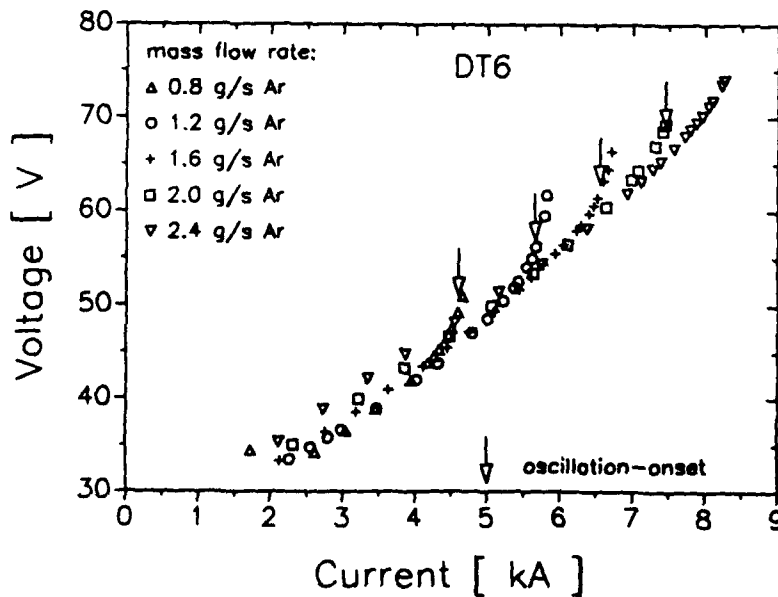


Fig. 2.13b: Voltage vs. current curves for the DT6-thruster at various mass flow rates

9
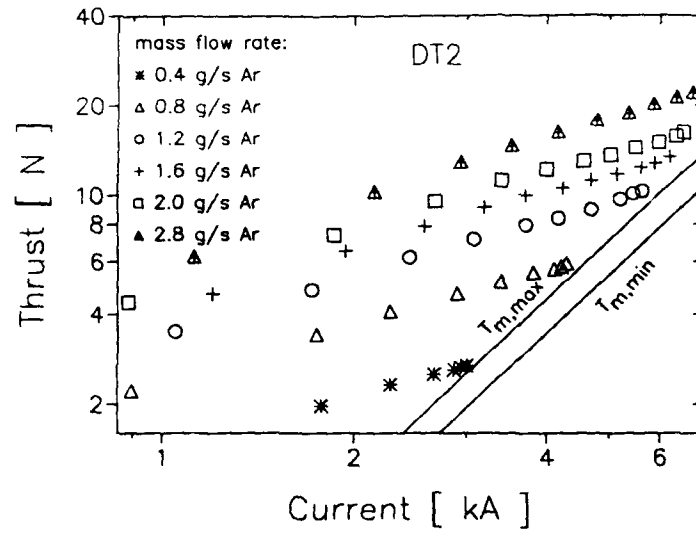
Fig. 2.14a: Thrust vs. current curves for the DT2-thruster at various mass flow rates
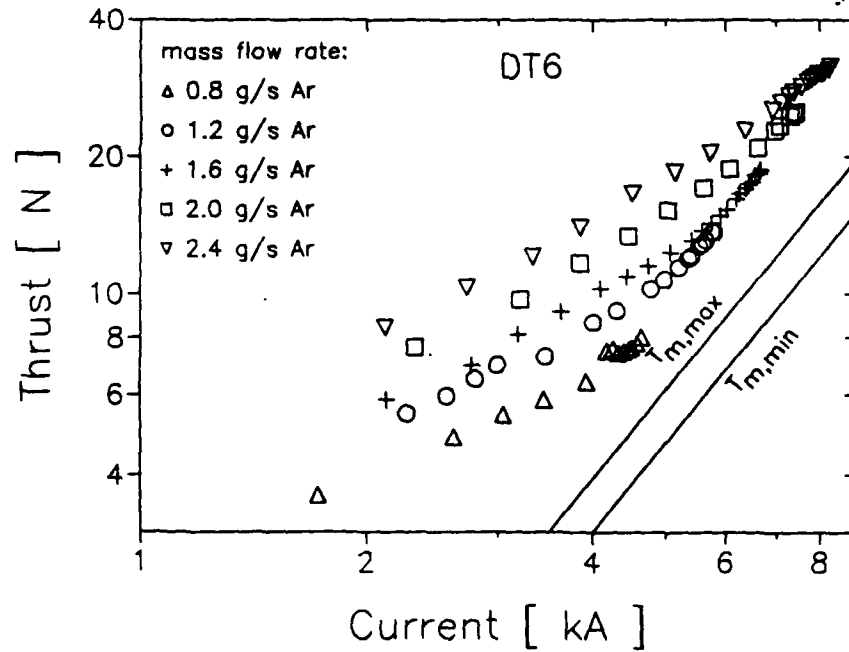


Fig. 2.14b: Thrust vs. current curves for the DT6-thruster at various mass flow rates
( These data for the DT6-thruster are preliminary )
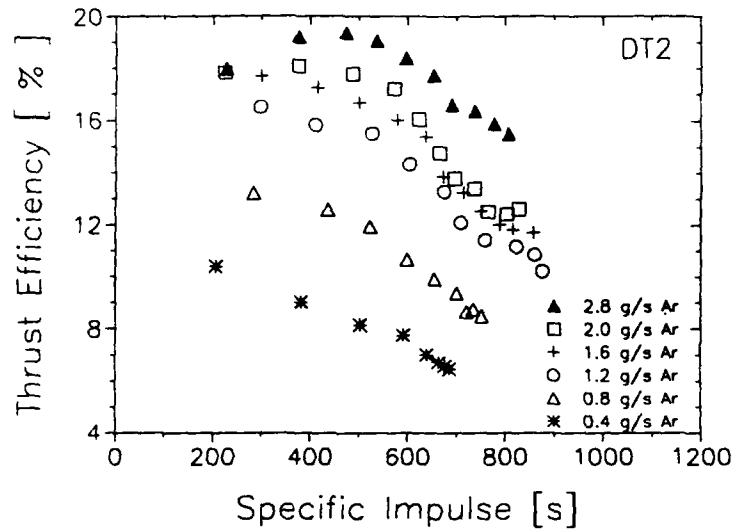
**Fig. 2.15a: Thrust Efficiency vs. specific impulse for the DT2-thruster at various mass flow rates**
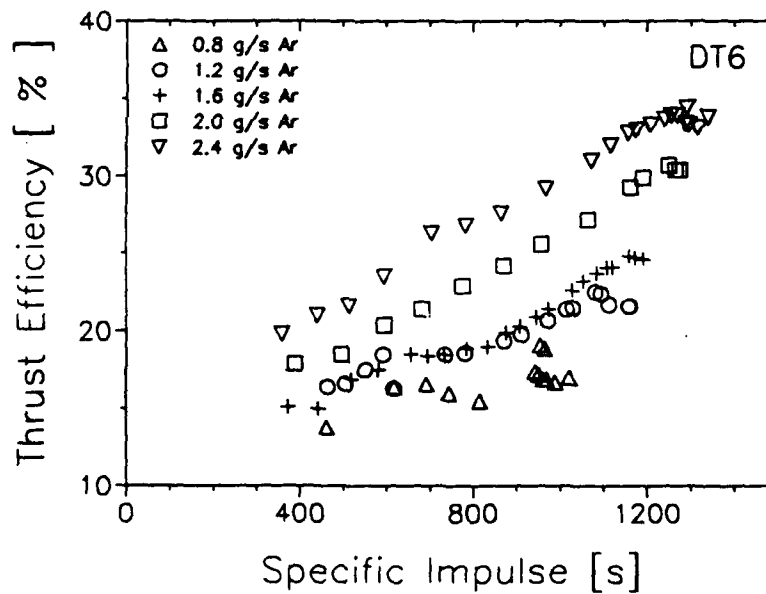


**Fig. 2.15b: Thrust Efficiency vs. specific impulse for the DT6-thruster at various mass flow rates**
**( These data for the DT6-thruster are preliminary )**

The investigation of the MPD-thruster HAT ("Hot Anode Thruster") (Fig. 2.16), which has a radiation-cooled anode could not be continued in this test period, because the anode cover, made of tantalum carbide, was damaged during a test when a water hose cracked. In the meantime, this covering sheath was renewed. So in a further research period, the HAT will be put on a thrust stand and hopefully the improvements in efficiency, caused by the lower discharge voltage (Fig. 2.17), can be verified.
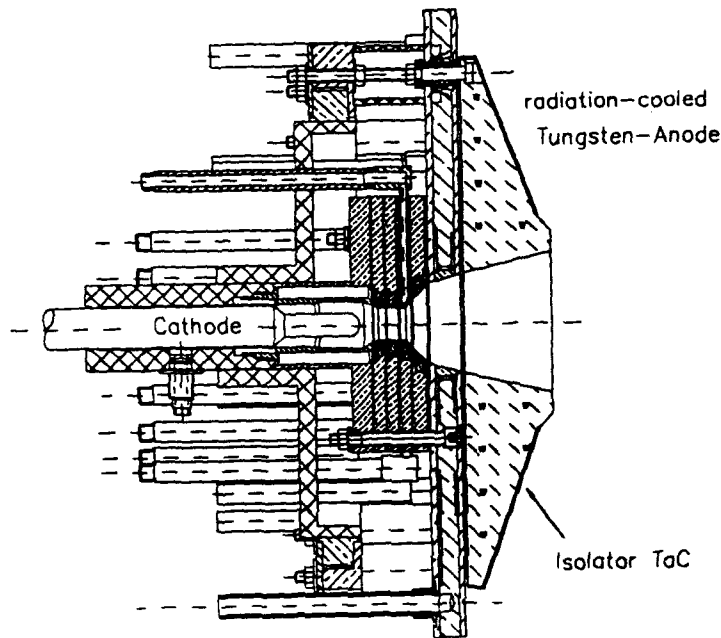


Fig. 2.16: Configuration of the " Hot Anode Thruster " ( HAT )
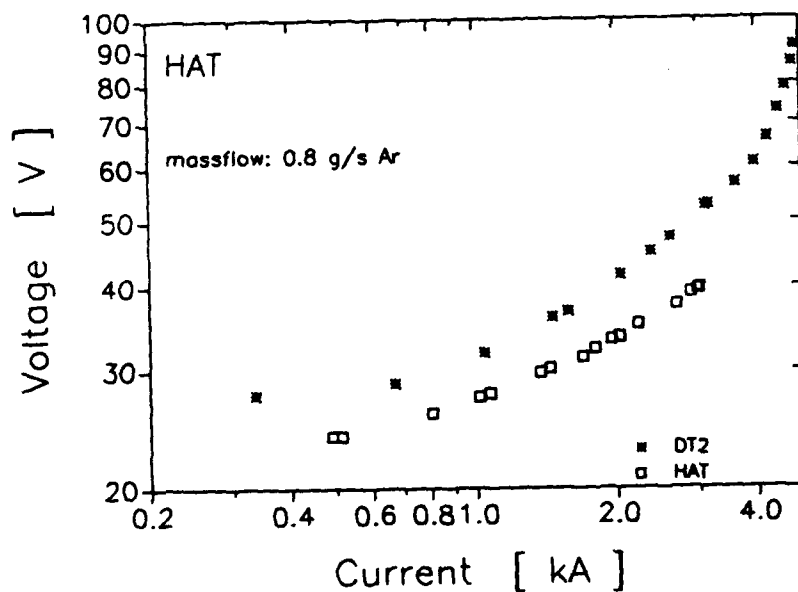


Fig. 2.17: Voltage vs. current curve of the HAT compared to the DT2-Thruster

# 3. Experimental results of the cylindrical MPD-thruster performance

Besides the nozzle type MPD-thruster, which are hybrids between pure MPD and thermal arcjet thrusters, a series of cylindrical MPD-thrusters ZT were designed. With these MPD devices, which should have a mainly radial current distribution and a low discharge voltage, an attempt was made to achieve a maximum magnetoplasmadynamic thrust and a low pinch effect at a certain power level.

The initial cylindrical MPD-thruster ZT1, shown in Figure 3.1, consists of three anode segments, a backplate segment and the thoriated tungsten cathode of 18 mm constant diameter, designed to be moved along the whole length of the discharge chamber. This discharge chamber has a diameter of 70 mm and a total length of 150 mm. Again the anode and insulator segments are made of watercooled copper. The current through each anode segment can be separately measured.
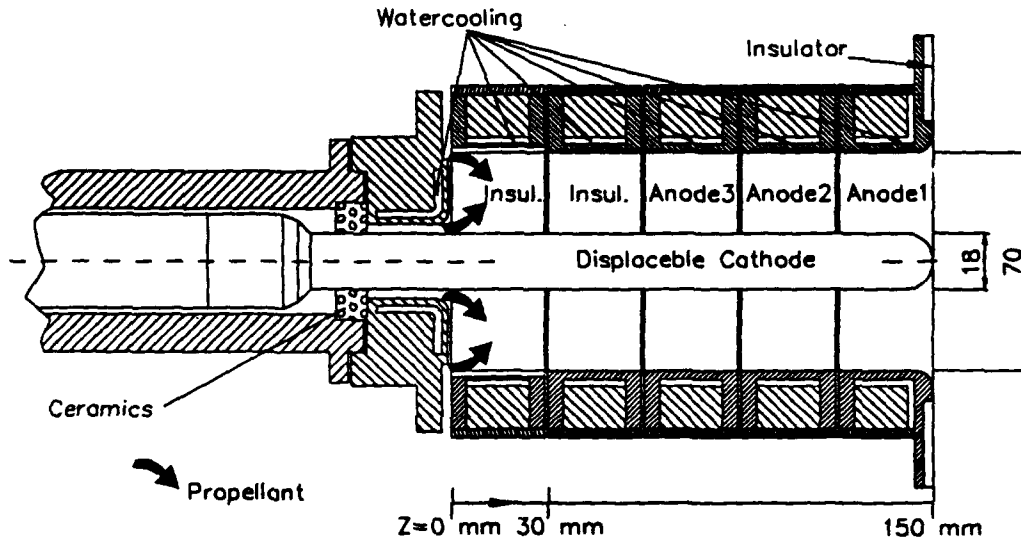


Fig. 3.1: Configuration of the cylindrical MPD-thruster ZT1
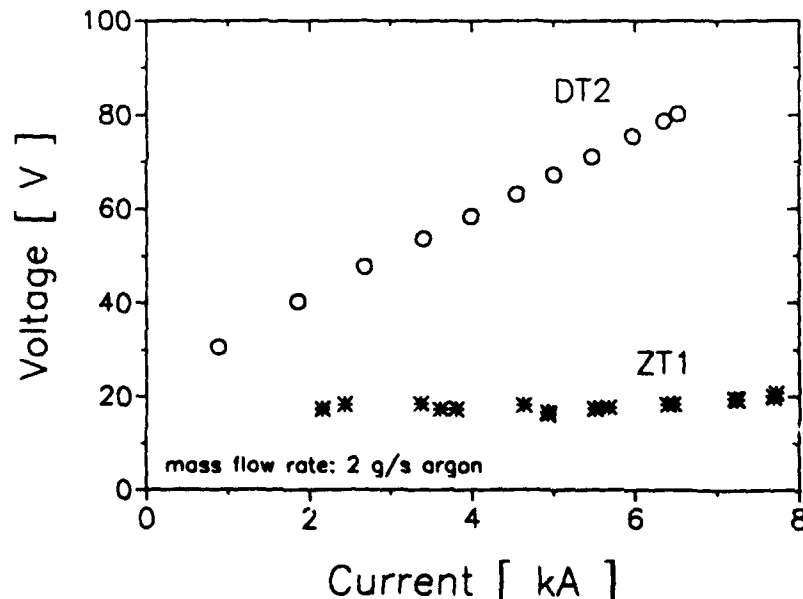


Fig. 3.2: Voltage-Current characteristic of the ZT1 and DT2-thruster, running with 2 g/s argon

13

The comparison of the voltage-current curves of the cylindrical ZT1 and nozzle type DT2-thruster in Figure 3.2 indicates, that in the case of cylindrical MPD-devices higher current values at low voltage levels can be reached. However, the tests with this cylindrical thruster were limited by high current damage of the cathode rod, a problem which has been encountered for all thruster geometries, the nozzle type MPD-thruster of the DT-series as well as the cylindrical thruster ZT1. At high current densities inside the cathode rod, the cathode material melted in the center of the cathode, not at the hot emitting tip as expected, but closer to an area, where the arc attachment is located just upstream of anode 3. Metallurgical investigations show that the melting seems to be influenced by a thorium migration under high temperature. The translation of the metallurgical report of the "Staatliche Material prüfanstalt Stuttgart, MPA", University Stuttgart was appended to the Process Report of Grant AFOSR-89-0535 dated February 1991 [11].

For the additional experimental investigation of the cathode damage, the ZT1 thruster was modified. A small optical system is fitted through a hole in the first insulator segment, where normally the plenum chamber pressure is measured ( Fig. 3.3). This is done in such a way that the lens is focused on the cathode surface. The purpose of the lens is to couple the light emission into a fiber optic, transmitting the light to a photo conductor pyrometer, this photo conductor pyrometer having previously been calibrated up to 2900°C. In addition to this temperature measurements 110 mm away from the cathode tip, where the damage is known to occur at high power levels, the temperature was also measured at the cathode tip by means of a Maurer TMR 85 Pyrometer, looking end on through a tank window ahead of the thruster position.
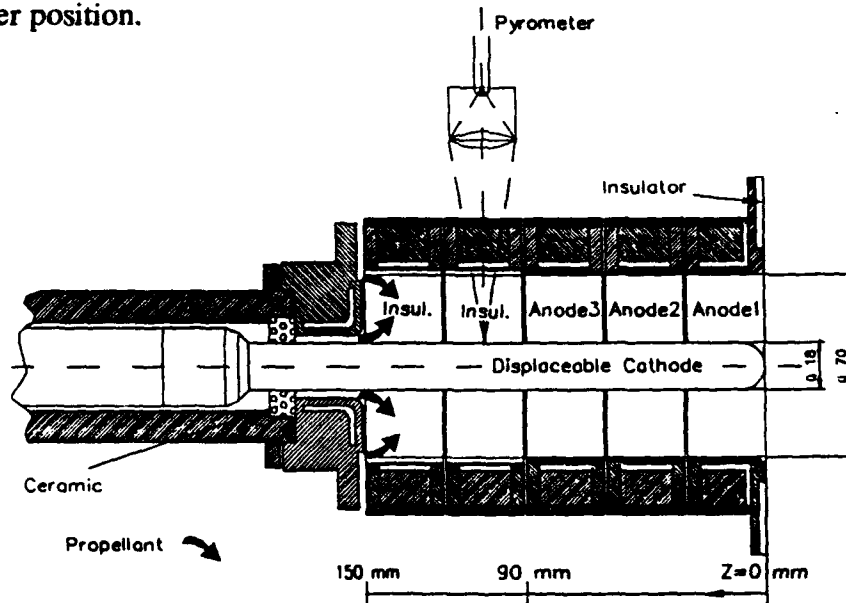


Fig. 3.3: Configuration of the modified cylindrical MPD-thruster ZT1
for temperature measurements of the cathode surface

Several tests measuring the temperature distribution on the cathode surface at different operation modes were carried out with this thruster. Fig 3.4 shows such a typical current versus time curve. At a constant mass flow rate of 2 g/s argon, the current was increased step by step from 2000 A during ignition to about 7500 A after 27 min.

14
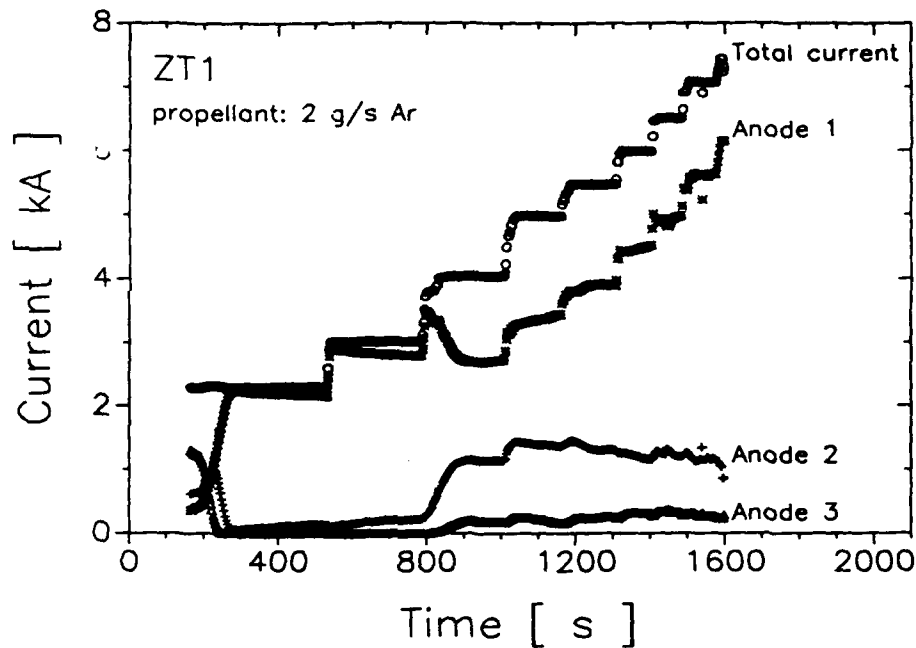
Fig. 3.4: Current vs. time curve of a typical run of the ZT1-thruster
with a mass flow rate of 2 g/s of argon

During ignition, the cathode is positioned in such a way that the tip protrudes about 10 mm from the back plate (z=140 mm) and the discharge current is set at about 2000 A. After a few seconds the thermionic emission of the discharge current is reached, the current stabilized and the thruster subsequently runs in the steady state phase. When the cathode is in a withdrawn position, most of the current goes into the third anode segment. While moving the cathode downstream (between 200 s and 300 s) the anode current attachment shifts to the front most anode ring. Leaving the anode in the same position and increasing the total current to 3000 A, a gradual spreading of the current onto the second anode ring starts. Once a total discharge current of approximately 3500 A is exceeded, a spontaneous distribution change to the advantage of the second and third anode segments takes place. From now on both currents will remain nearly constant although the total current is increased. The gradual distribution separation seems to be due to a slow enlargement and backward movement of the arc attachment region at the cathode.

In Figure 3.5, the temporal development of the temperatures at the cathode tip and the cathode surface at 110 mm upstream, starting after the positioning of the cathode, is depicted. At first, when most of the current goes into anode segment 1, the temperature at the cathode tip is much higher and decreases while the current distribution change takes place. Here the temperature at 110 mm cathode position overcomes the cathode tip temperature and keeps on increasing with the current raise. The test has to be stopped when 2900°C are reached, firstly because the limit of the pyrometer was reached and secondly because of the risk of once again causing the cathode to melt, thus destroying it, since it has to be assumed that the temperature in the core of the cathode is higher than on the surface.

These temperature measurements point out clearly phenomena which occur with the steady state ZT-thrusters. On the one hand the arc does not attach at the round cathode tip, noticeable also at the darker surface there, but attaches immediately behind this tip zone. The arc attachment region is slowly enlarging and moving backwards with higher current levels. The high temperature values in the backward part of the cathode are caused by the high

15

current densities and hence Joule heating inside the cathode rod which decrease in the arc region.

Because the insulator segments can be exchanged, we will be able to measure the temperature at various points of the cathode surface, allowing in future the development of a temperature model of the cathode.
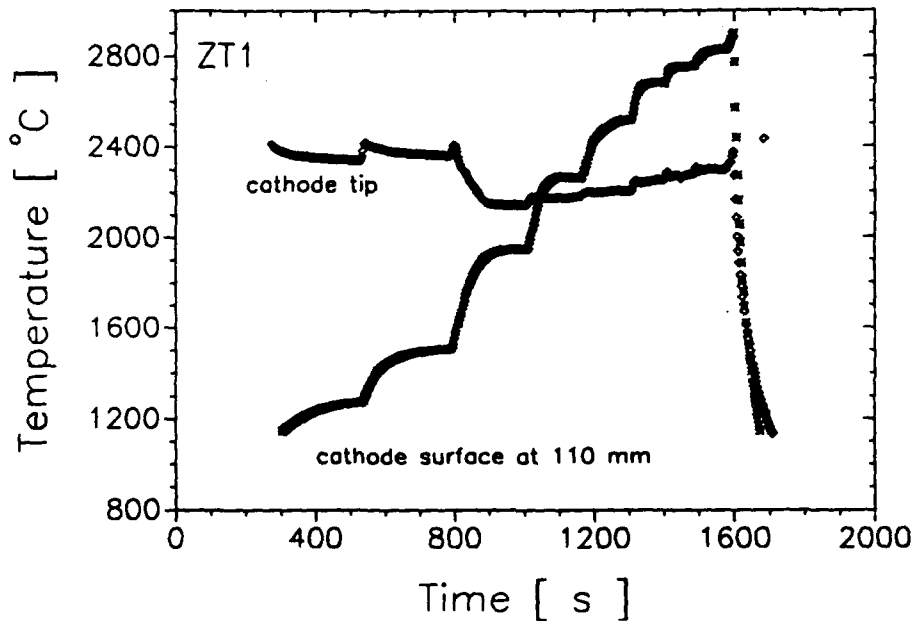


Fig. 3.5: Temporal temperature curves of the ZT1-Thruster
during the current raise shown in Figure 3.4.

To counterbalance this thermal damage effect, a new thruster with a modified cathode geometry was designed (Fig. 3.6). In the backward part of this new thoriated 2% tungsten cathode the diameter was enlarged to 40 mm with a subsequent conical reduction in diameter in the anode region, so that the tip has a radius of 10 mm. The 150 mm long cathode itself weighs 4 kg.

The anode segments 2 and 3 and also the neutral plenum chamber segments were taken from the ZT1−thruster. Merely the first anode segment was designed newly, to guarantee a better water cooling. The discharge chamber diameter was kept constant at 70 mm. Also the back plate segment was adapted to the new cathode geometry. Because the distance between cathode surface and the plenum chamber in the back part is only 15 mm, the propellant is only injected near the cathode, in contrast to the former cylindrical thrusters, where also propellant was injected near the plenum chamber wall. The cathode of the ZT3−thruster can be fixed in different positions, but a displacement during the test cycles is not possible. During the first tests, described in this report, the cathode tip was positioned in the anode exit plane.

16
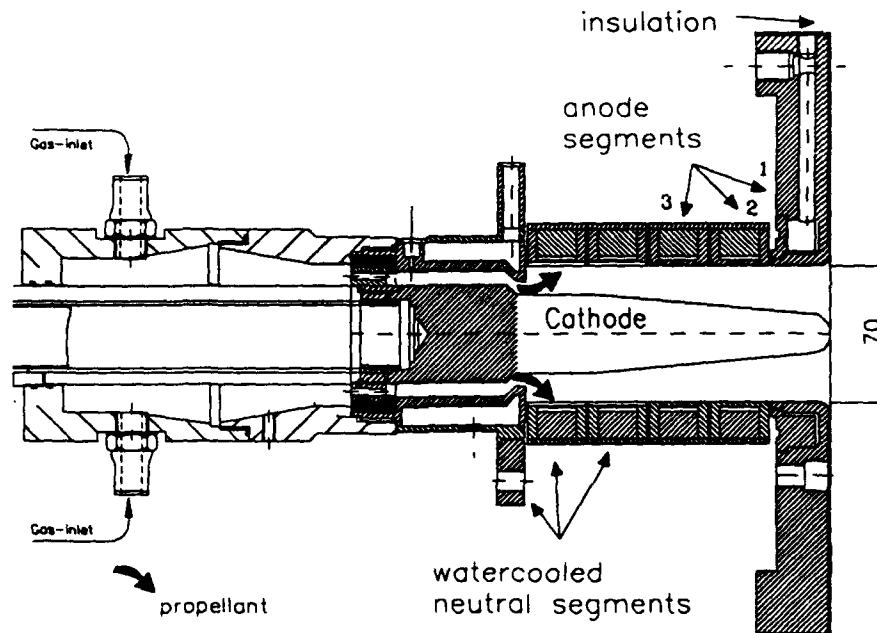
Fig. 3.6: Scheme of the newly designed ZT3-thruster.

At the same time a new thrust stand for the cylindrical thrusters was installed in the vacuum tank number 3. This tank has a diameter of 2 m, a length of 2.5 m. The thrust balance corresponds in principle with the one used for the nozzle type thrusters. By means of an improved water-cooling system with enlarged cross-section of the current supply bars, tests at higher current levels can be performed without problems.

At the high current tests, however, the induced magnetic field effects caused between the solid conductors placed on and outside the movable balance cannot be neglected anymore and result in a pseudo thrust. Short circuit thrust measurements were performed up to 15 kA, shown in Figure 3.7. These measured thrust values have to be subtracted from the measured thrust values during the test cycles. The larger error bars at high current levels are probably due to boiling of the mercury in the baths. For future tests at high current levels, the mercury has to be better cooled, also to prevent a contamination of the vacuum tank and system.
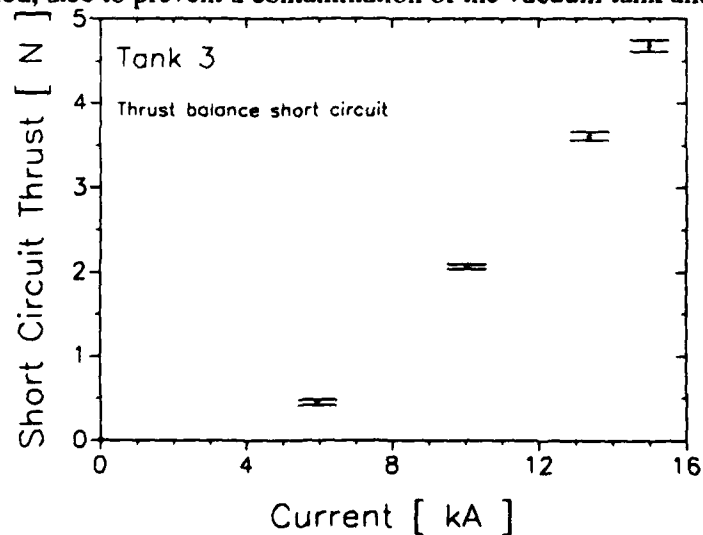


Fig. 3.7: Short Circuit Thrust of the thrust balance for the cylindrical thrusters

In the following diagrams, the experimental results of the first runs of the ZT3-thruster are presented. The thruster was ignited with a Paschen breakdown at a set current of about 2000 A and a mass flow rate of 2 g/s argon. The ignition phase, determined by the cold cathode and by a spotty arc attachment on the cathode surface, takes about 10 - 15 s, followed by the transition to the thermionic mode. The first tests showed, that one has to raise the current fast to more than 4000 A, because below this current level the thermionic heating of the cathode is not strong enough, so that the arc attachment zone moves periodically back-and forth on the cathode. Above 4000 A the thruster runs very stable and no oscillation or unsymmetry could be observed. In Figure 3.8 the current-voltage dependence of the ZT3-thruster is compared to the results of the DT6-thruster, both running with 2 g/s argon.
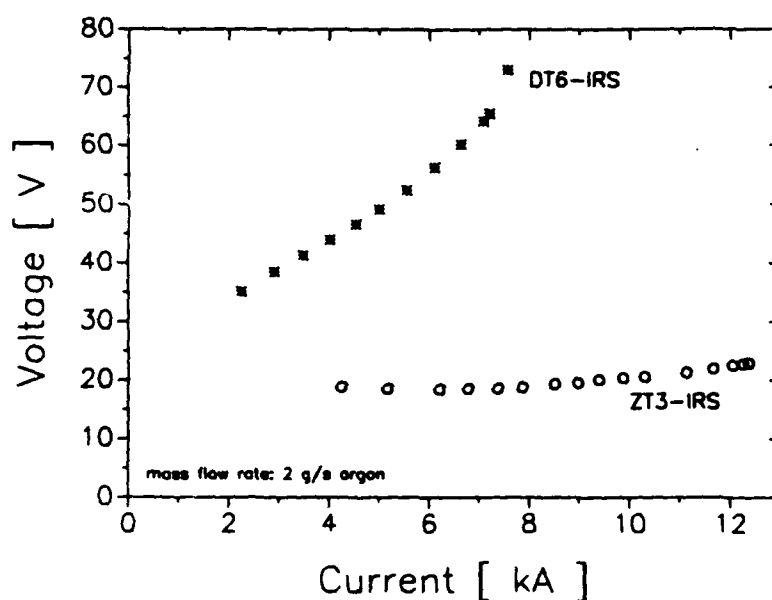


**Fig. 3.8: Voltage-Current characteristics of the ZT3-thruster**

The comparison of both characteristics shows, that again the voltage of the cylindrical thruster is moderately low and increases only very slowly with the current, while the curve for the nozzle type thruster steeply rises. At about 7450 A the plasma instabilities occur for the DT6-thruster, what is also recognizable by the additional ascent of the voltage. For the ZT3-thruster no indication for the occurence of instabilities could be detected up to 12.7 kA.

Here an $I^2/\dot{m}$ - value of more than $8 \cdot 10^{10} A^2 s/kg$ was reached. The critical $I^2/\dot{m}$ - value for the DT6-thruster for the same mass flow rate is about $2.7 \cdot 10^{10} A^2 s/kg$.

In Figures 3.9 and 3.10 the results of the thrust measurements and the calculated thrust efficiency vs. specific impulse characteristics are presented.

18

Fig. 3.9: Thrust vs. current curve for the ZT3-thruster, running with 2 g/s argon



Fig. 3.10: Thrust efficiency as a function of specific impulse of the ZT3-thruster,
running with 2 g/s argon

The thrust increases with the curre . and reaches about 10 N at 12.7 kA. Also the calculated thrust efficiency rises linear with the specific impulse. At maximum current a specific impulse of 525 s and an efficiency of 9% were reached This makes it clear. that the ZT3-thruster with this geometry must be operated at much higher current levels, the more so since the power level was not more than 300kW. The current distribution on the different anode segments could not be exactly determined, but during these first tests most of the current went into the first anode segment.

Besides the thrust and other operation parameters, the heat losses of each thruster segment was determined, measuring the water flow rate and the temperatures of the in and outgoing water. In Figure 3.11, the heat losses are compared to the total input power of the ZT3-thruster. It shows that again more than half of the input power is lost by heat transfer to the thruststream mainly to the anode. Therefore also the thermal efficiency is below 50%, slowly decreasing with the higher current (Fig. 3.12).

**Fig. 3.11: Comparison of power input and heat losses of the ZT3-thruster**
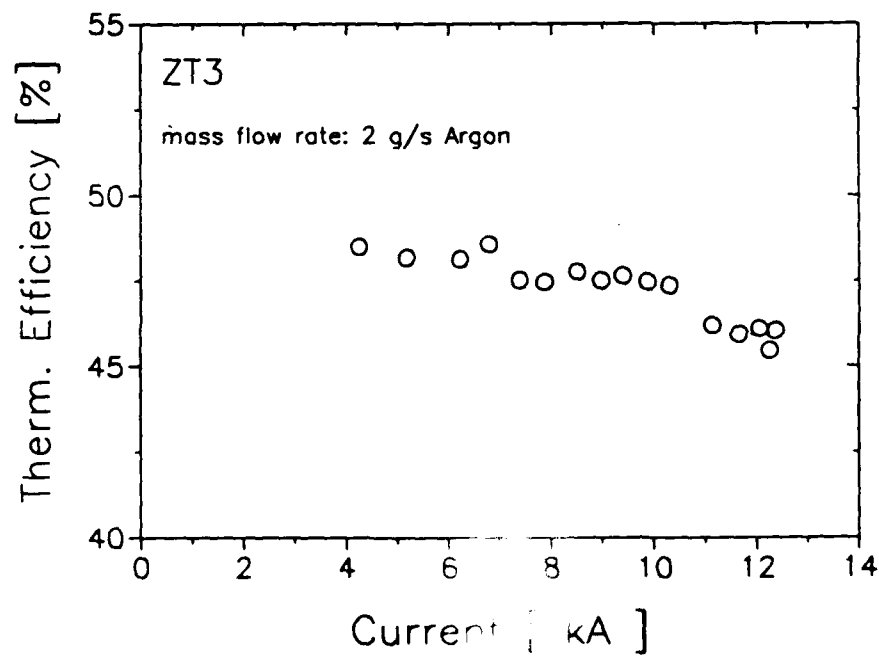


**Fig. 3.12: Thermal Efficiency vs. current of the ZT3-thruster, running with 2 g/s argon**
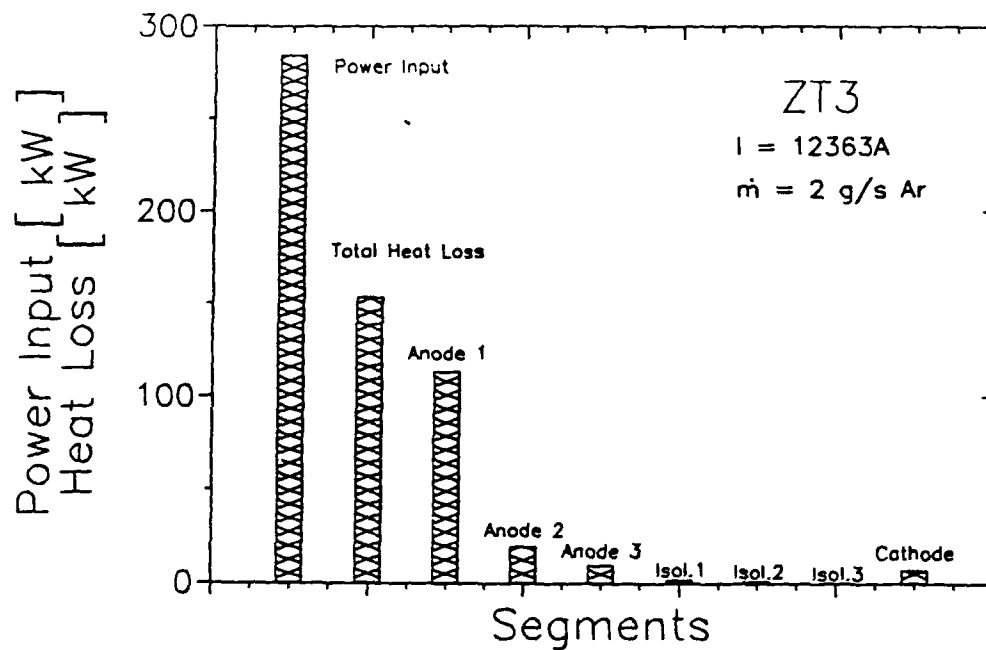
**Fig. 3.13:** *Distribution of Heat Losses of the ZT3-IRS at high current level*

The distribution of the heat losses in the thruster segments at 12.6 kA (Fig. 3.13) shows that nearly 75% are lost at anode 1. This heat distribution corresponds well with the current distribution and signifies that for these first tests the arc attaches at the first anode segment. On the contrary the thermal load of the insulator segments is neglectful, indicating that the arc attachment zone is restricted to the front part.

Future tests with lower mass flow rates at high current levels are planned, hopefully resulting in better performance data, and to investigate high current limits of this thruster geometry.

## 4. Plasma Diagnostics

### 4.1 Electrostatic probe measurements

Electrostatic probes [12−14] are used to determine the electron temperature $T_e$ and electron number density $n_e$ at different axial and radial positions in the argon plasma plume of the MPD−thrusters DT.

An electrostatic (Langmuir) probe consists of a metallic electrode placed inside a plasma. The measurement method is to obtain a voltage−current characteristic for single−and double probes. For single probes, a metallic part inside the vacuum chamber is used as reference electrode [15], whereas for double probes two electrodes of equal or different areas are used. While one electrode is biased to draw ions, the second electrode collects electron current. The experimental setup for double probe measurements is shown in Fig. 4.1. For electrostatic double probes two electrodes have been separated by a certain distance $d$, so that they do not disturb each other, $d > l_d$, $l_d$ being the Debye−length. Although it is not necessary to use probes with the same area exposed to the plasma, for $T_e$ determination it is most convenient to use symmetric electrodes, for which symmetric characteristics are then obtained.
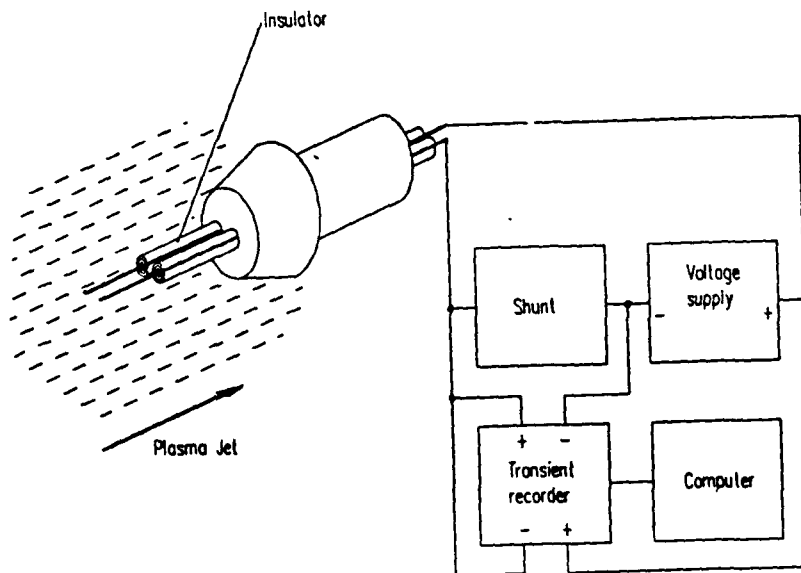


Fig. 4.1: Experimental setup of double probe

To operate a double probe, a ramp voltage difference is applied between the two electrodes. The electrode which is most negative reaches ion saturation due to the lower ion mass. From the slope of the current to the double probe at the "floating potential" $V_f$ and from the extrapolated ion saturation currents, the electron temperature $T_e$ can be obtained. The number density of charged particles can be calculated by the adapted equations for single probe application which are valid for plasmas generated with DT−thruster series [16]. Single probes require a Maxwell distribution of the electron energies for the evaluation of the electron temperatures, but this cannot be guaranteed close to the thruster. Therefore the measurements were taken with double and triple probes. The triple probe is an electrostatic probe system which allows an immediate direct display of the electron temperature and

electron number density without intensive characteristic evaluation [16, 17]. The electrostatic triple probe consists of three symmetrical electrodes of equal surface areas, two of them connected as a double probe and a third one floating with the plasma potential. By moving this probe through the plasma, direct radial and axial distribution of $T_e$ can be measured. From the collisionless probe theory and the measured current I in the double probe circuit, the electron number density is determinable. Electrostatic triple probes are currently to be verified for diagnostics in MPD generated plasma jets. Previous investigations by other authors already showed good results [17]. The application of electrostatic probe methods is limited and characterized by the particles mean free path $I_{ei}$ and the Debye−shielding length $I_d$. In the case of the argon plasma generated by the IRS−MPD thrusters, the mean free paths are calculated to be much larger than the Debye−length $(I>>I_d)$ and therefore the plasma can be treated as a collisionless one.

For the determination of electron temperatures and electron number densities several measurements per test point with a double probe and a triple probe were performed. The measurements were taken at axial positions of 50, 150, and 300 mm with the double probe aligned with the plasma stream. The alignment of the probe is required in order to avoid effects on the measured currents, caused by the directed particle flows to the probes at angles of incidence [ 18−20 ]. The results shown are average values, the error bars are standard deviations. The length of a cylindrical double and triple probe aligned with the plasma stream was 10 mm, with electrode diameters of 0.4 mm. In Figs. 4.2 and 4.3, the axial distributions of electron temperature in the centerline of the Argon plasma jet are shown for different currents and massflow rates of 0.8 g/s and 1.6 g/s argon. The calculated electron number densities are shown in Figs. 4.4 and 4.5.

The electron temperature in the plasma centerline increases with the mass flow rate. The high values of the electron temperature close to the anode are planned to be verified by optical methods in the near future. The electron number density of about $10^{13}$ to $10^{14}$ cm$^{-3}$ is calculated by assuming only single ionized argon atoms.
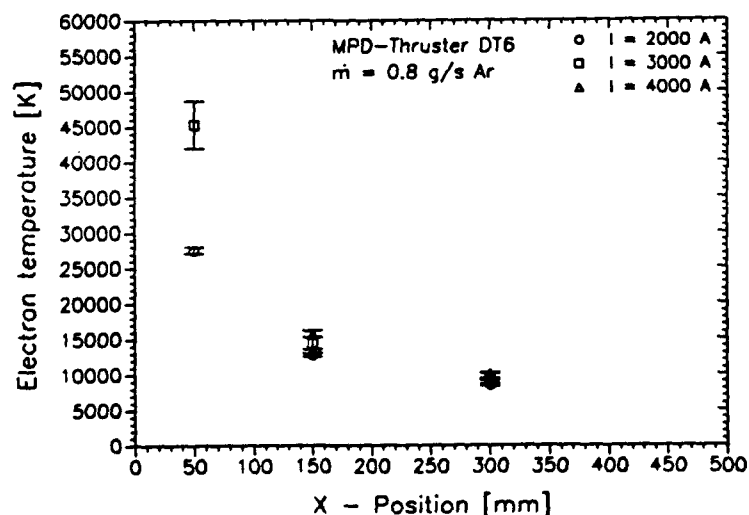


Fig. 4.2: Axial electron temperature distribution, 0.8 g/s Ar, double probe
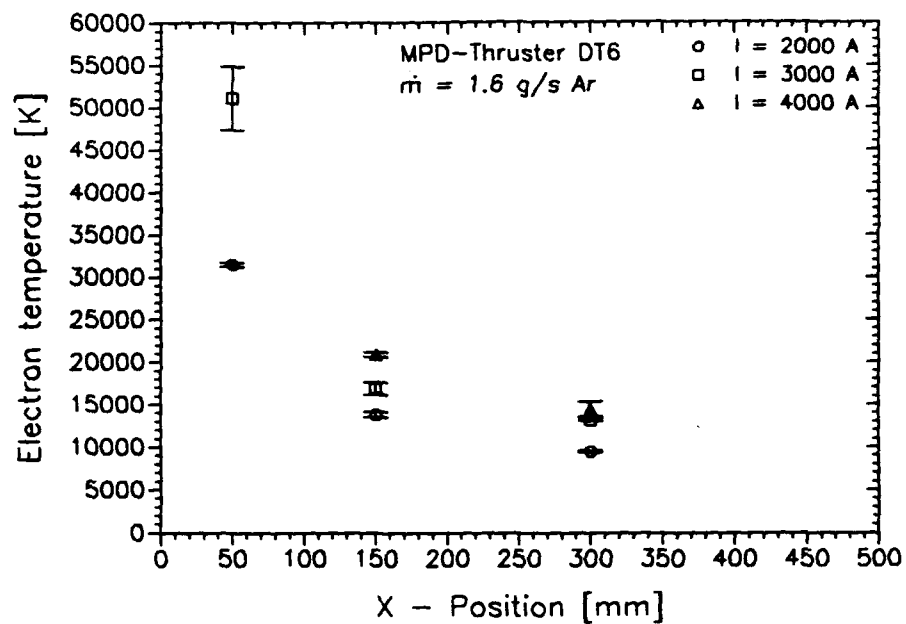
Fig. 4.3: Axial electron temperature distribution, 1.6 g/s Ar, double probe
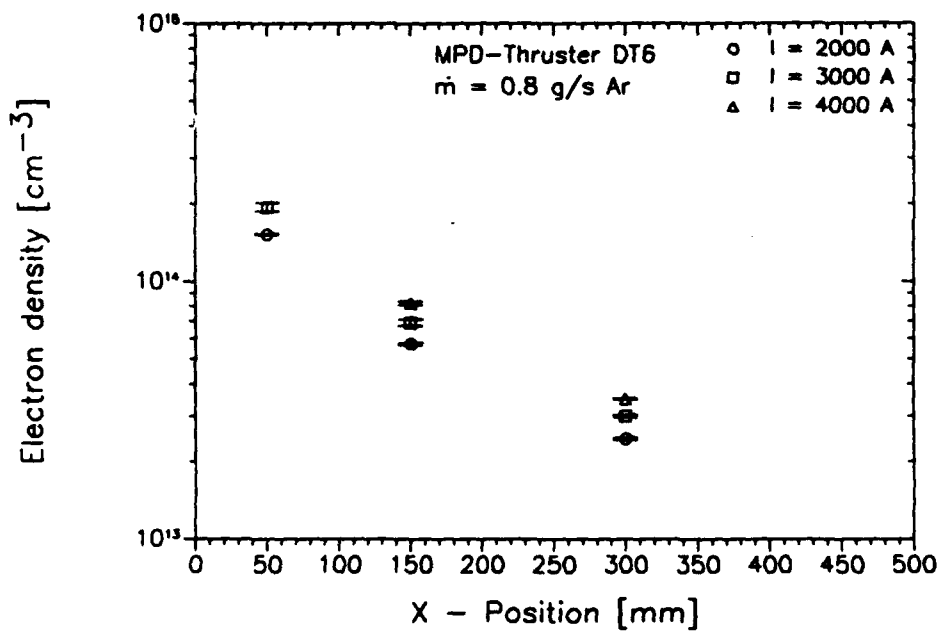


Fig. 4.4: Axial electron number density distribution, 0.8 g/s Ar, double probe

24
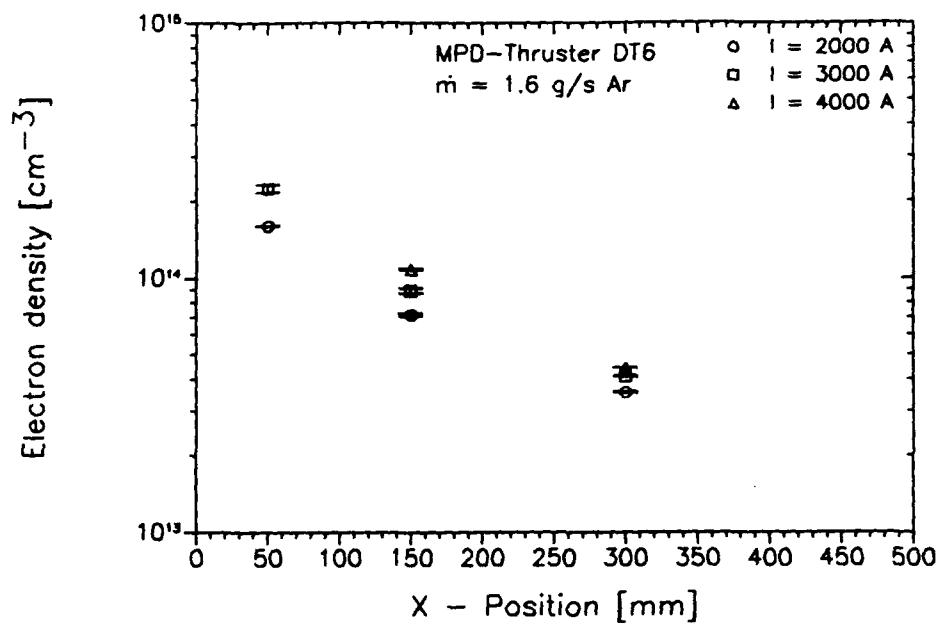
Fig. 4.5: Axial electron number density distribution, 1.6 g/s Ar, double probe

In Fig. 4.6 and 4.7 the radial distributions of the electron temperature and electron number density measured with a triple probe at an axial distance of 100 mm are shown.
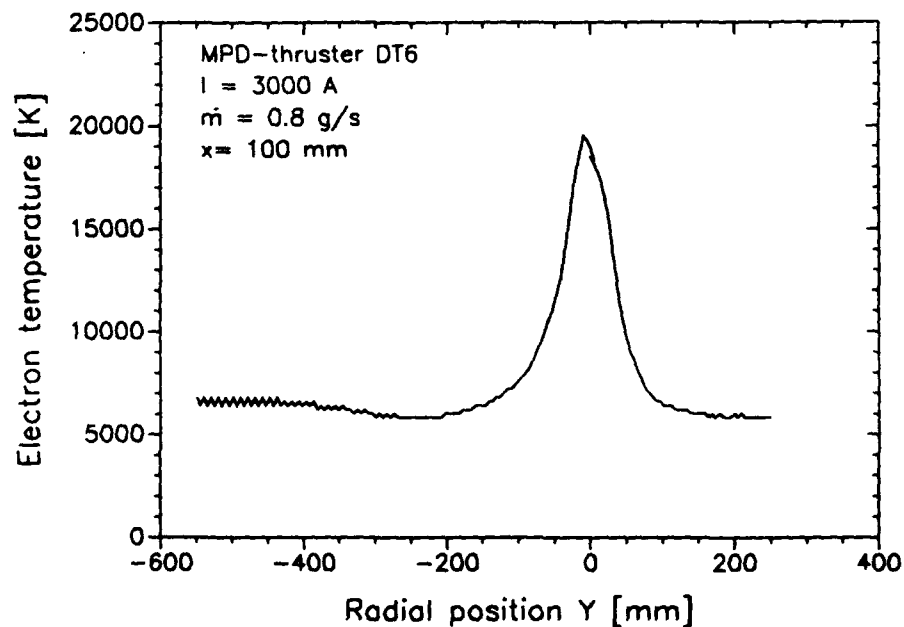


Fig. 4.6: Radial electron temperature distribution, 0.8 g/s Ar, triple probe
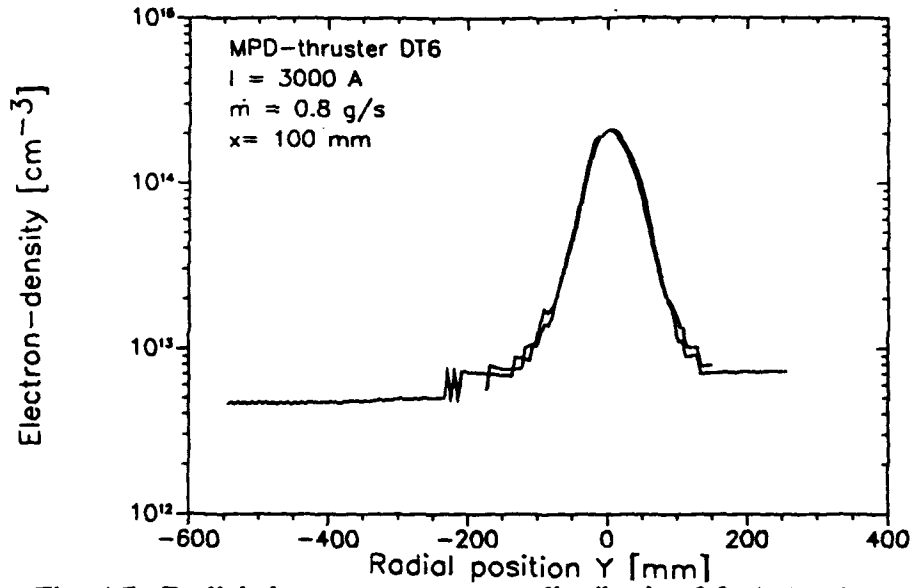
Fig. 4.7: Radial electron temperature distribution 0.8 g/s Ar, double probe.

The values in the plasma centerline correspond well with the values extrapolated from the double probe measurements at the position of 100 mm.

## 4.2 Fabry−Perot−Interferometry

The Fabry−Perot Interferometry (FPI), a nonintrusive optical diagnostic technique is a special form of emission spectroscopy using the high resolution of the Fabry−Perot interferometer for a detailed investigation of single emission lines [ 21 ]. By detecting the Doppler shift $Dl_D$, which occurs when an emitting particle of high velocity does not move perpendicular to the optical axis of the setup, and the Doppler line broadening $Dl_{Tr}$ caused by thermal motion of the emitting particles, the particles velocity $v_{PL}$ and translational temperature $T_{tr}$ can be determined [22, 23 ]. The experimental setup is shown in Fig. 4.8.
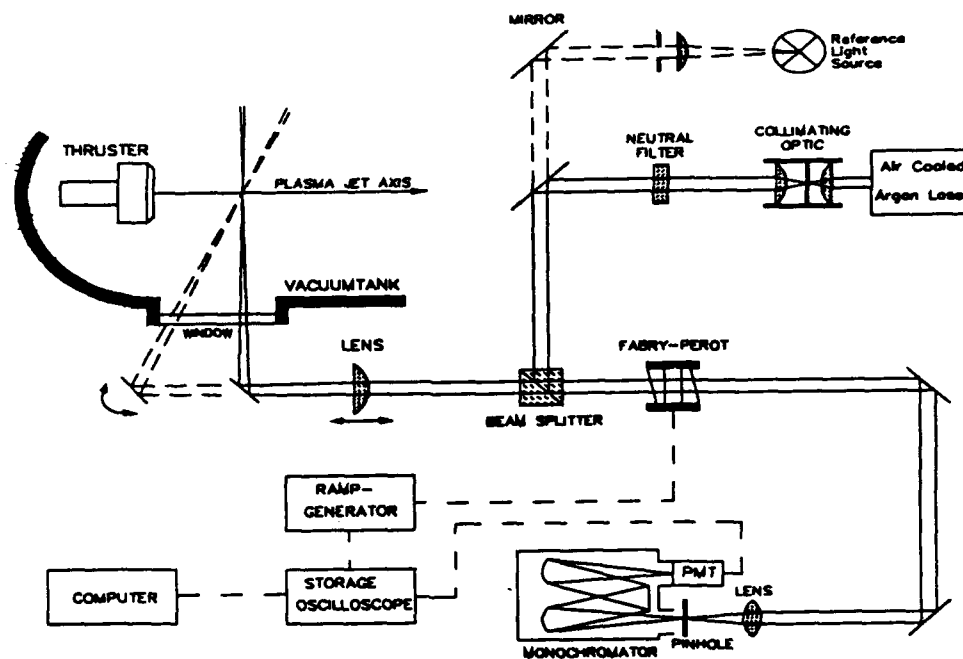
Fig. 4.8: Experimental setup of the Fabry-Perot Interferometrie

The experimental setup is completely outside the vacuum tank. The selection of the wavelength $\lambda$ transmitted through the interferometer is linearly dependent on the refractive index n and the spacing d between the mirror plates of the interferometer. Since the refractive index n is set to 1 for the air between the mirror plates, any wavelength can be transmitted by varying the plate distance d. The fine tuning and scanning of the mirror spacing d is performed by piezoelectric elements. The intensity of the emission line investigated with the Fabry–Perot–Interferometer is transformed to a voltage signal by a fast single channel photomultiplier.

For argon investigations the specific $Ar_{II}$ emission line at 488 nm was chosen. The line is within the transmission range of the interferometer from 400 to 800 nm. With the given values of a reflectivity of 94%, a mirror flatness of 1/200, a focal length of 300 mm for the lens behind the interferometer and a pinhole diameter of 0.6 mm, the finesse, which is a measure of the interferometer's ability to resolve closely spaced emission lines, and the resolvable bandwidth $Dl_{FWHM}$ were calculated to be about 43 and 0.008 nm respectively for a mirror separation of 3 mm. The mirror separation and therefore the resolution of the interferometer was chosen according to a theoretical calculation of the Doppler shift at the expected velocities. An argon ion laser was used as an unshifted monochromatic light source. The heavy particle temperature was determined from the Doppler broadening at perpendicular incidence, errors are in the range of up to $\pm$ 20% due to the FWHM determination by a Fit function [24, 25 ]. Figure 4.9 shows integrated results at an axial distance of 180 mm to the MPD–thruster DT2 for a massflow rate of 0.8 g/s and 4000 A thruster current. Those integrated results are to be transformed into local values of velocity and temperature by an Abel inversion technique [22].
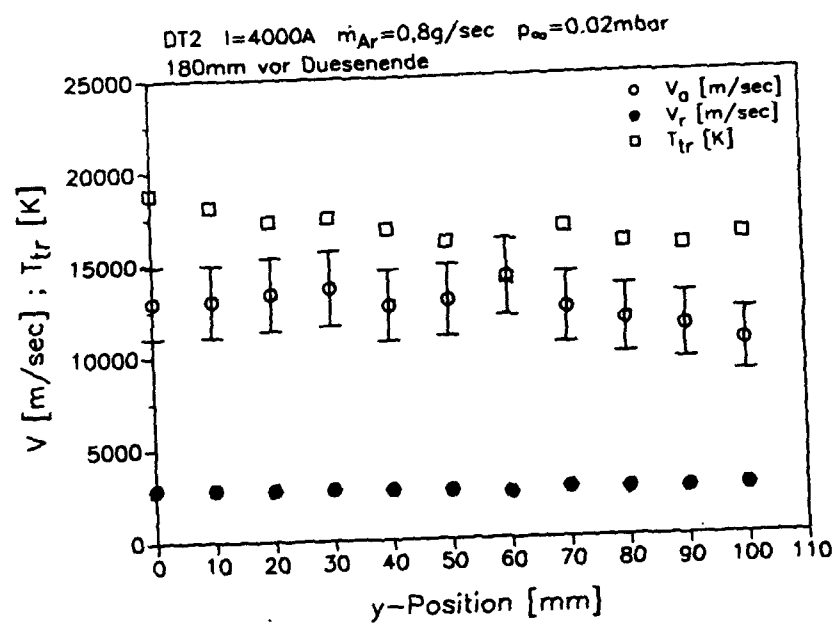
Figure 4.9: Radial profiles of the translational heavy particle temperature and the plasma velocity measured with FPI

## 5. The Onset of plasma instabilities

As mentioned above the magnetoplasmadynamic thruster reaches an unstable mode at high power levels: the voltage versus current curve rises steeply and therefore the thrust efficiency decreases. At a current level somewhat above the break in the voltage curve, the beginning of an unstable behavior of the arc discharge and the plasma can be noticed. Oscillations were detected with an electrical probe and analyzed by a faster fourier transformation to get the frequency spectrum. Figure 5.1 shows as example such an oscillation spectrum for the DT2-Thruster, running with 0.8 g/s argon at a current level of 4962 A. The detected frequencies are in the several 100 kW and in the 1.5-2 kW range.
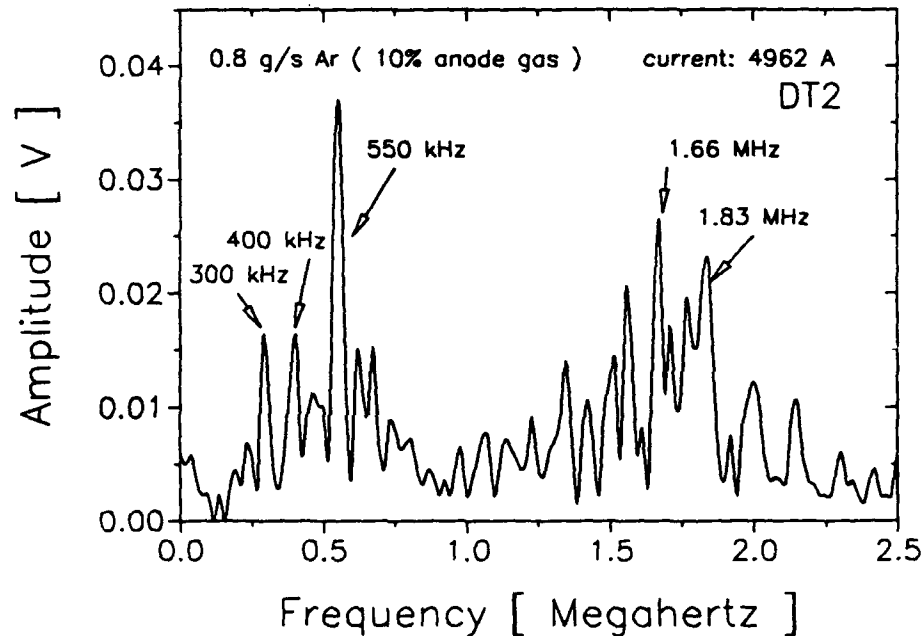


**Fig. 5.1: Frequency spectrum of plasma oscillations at the DT2-Thruster**

These instabilities were accompanied by a strong rise of the anode fall voltage ( Fig. 5.2 ), which can be determined approximately from the heat balance at the anode. The total anode heat loss $\dot{Q}_A$ is caused by the ohmic heating in the anode sheath, translation energy and "entry" energy transport of the electrons and convective heating, neglecting radiation:

$$\dot{Q}_A = ( U_A + 5/2 \, k \, T_e + \Phi + U_{conv} ) \cdot I$$

The following assumptions were made:
- for the electron temperature was taken 15000 K extrapolated from probe measurements
- for the work function of copper: 4.62 V
- the convective heat transfer at the anode was determined approximately from the heat loss of the neutral segment next to the anode.

The arrows in figure 5.2 mark the current values, where of the oscillations can be detected on the oscilloscope. Figure 5.3 shows the dependence of the corresponding critical currents, called onset current, on the mass flow rate, an almost linear function.

Reducing them according to the correlation factor $A = I^2/\dot{m}$, the correlation for the nozzle type thrusters is determined to:

$$A_{crit} = 2.4 \cdot 10^{10} \, A^2 s/kg$$

With this value, the onset current is calculated and also depicted in Figure 5.3. It fits very well with the measured curve, indicating that this $A_{crit}$ is almost a constant for this thruster.
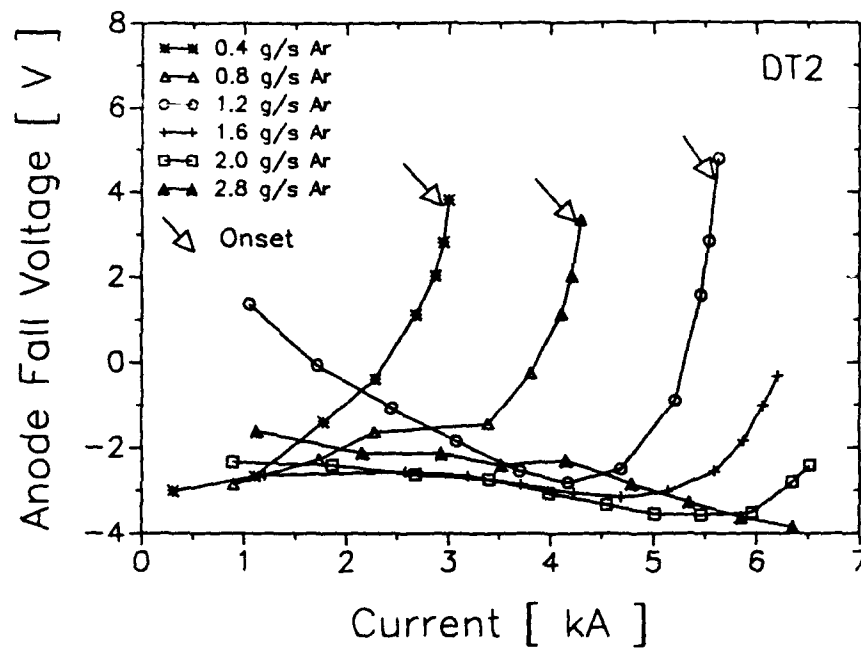
**Fig. 5.2: Anode fall voltage vs. current for the DT2-thruster for various mass flow rates**
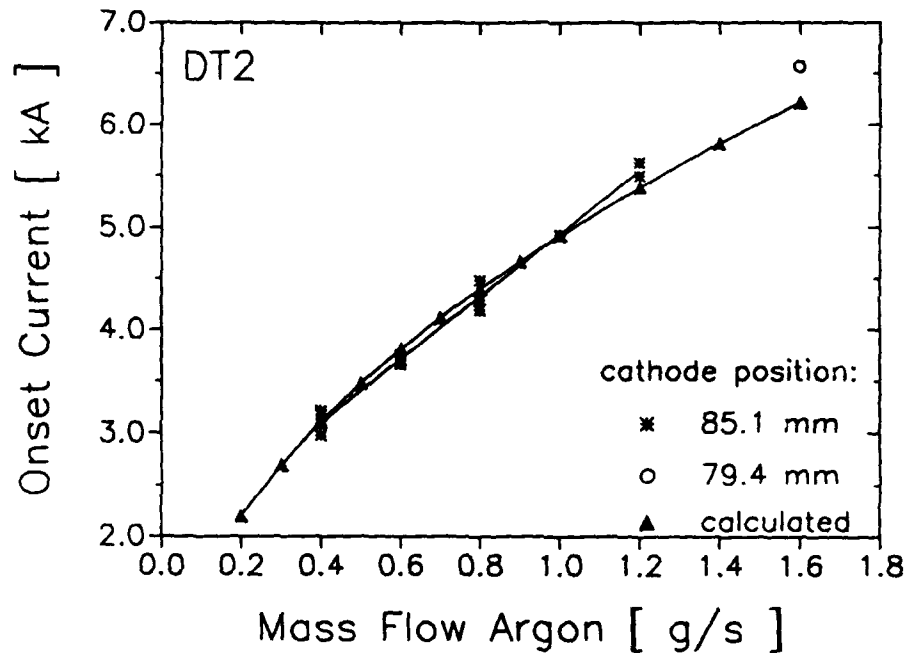


**Fig. 5.3: Onset current vs. mass flow rates for the DT2-thruster**
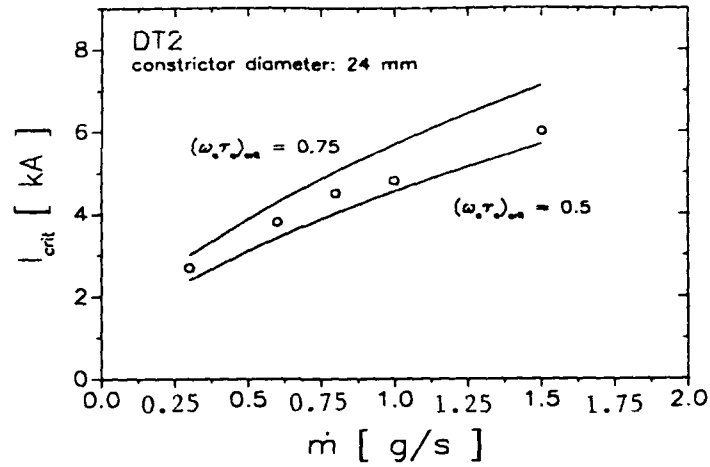
**Fig. 5.4a: Critical current vs. mass flow rate for the DT2-thruster**
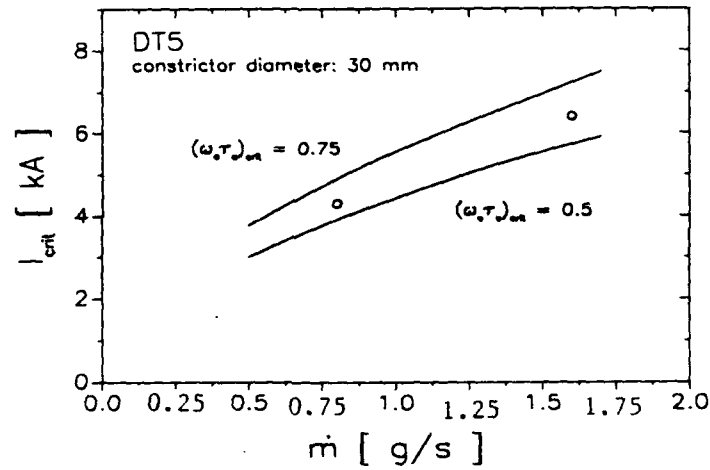


**Fig. 5.4b: Critical current vs. mass flow rate for the DT5-thruster**
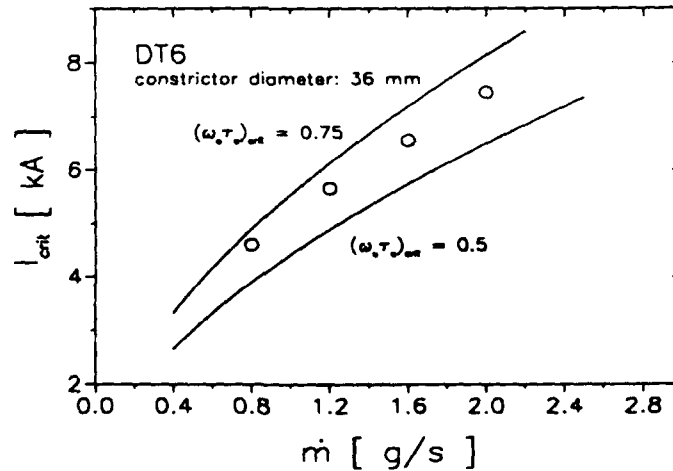


**Fig. 5.4c: Critical current vs. mass flow rate for the DT6-thruster**

In Figures 5.4 a–c again the currents $I_{crit}$ are given as a function of mass flow rate for the different nozzle type thrusters. To compare the experimental results with numerical calculations for the onset conditions, also $I_{crit}$ as function of m calculated according to the requirements:

$$7.65 \cdot 10^{-10} \, f^* \, r_c^{\frac{1}{5}} \frac{I^{\frac{9}{5}}}{\dot{m}_c} \leq ( \, \omega_e \, \tau_e \, )_{crit}$$

with $( \, \omega_e \, \tau_e \, )_{crit}$ –values of 0.5 and 0.75 are plotted as lines in these diagrams. The above requirement results from new qualitative and also quantitative explanation of the onset phenomenon, which is based on a run–away Joule heating process caused by the self–magnetic field of a current carrying plasma channel, drastically decreasing the radial conduction heat loss. The consequence is a contraction of the discharge cross section which leads to an unstable plasma behavior resulting in a helically shaped discharge channel within the nozzle part of the thruster as shown in Fig. 5.5. The complete theory of this stability criterion is given in the Final Scientific Report " Basic Processes of Plasma Propulsion", dated April 1992 [9, 26 ].
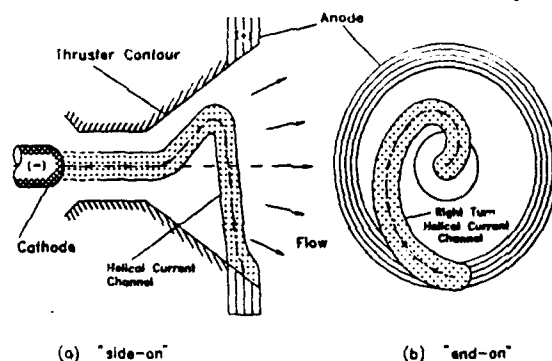


Fig. 5.5: Helical discharge channel within the nozzle

Measurements with a CCD–camera which allows exposure times of $< 100$ ns also indicate that near the onset of unstabilities the discharge seems to be confined to a smaller channel which moves around rapidly. The arc attachment on the anode can be observed in photographs in Figure 5.6. Unfortunately the single exposure time does not allow enough data to conclude that there is a rotation, much less to determine a frequency for the possible rotation. Therefore new measurements with a faster camera and with magnetic pick–up probes are planned.

Spectroscopic investigations near the onset conditions showed the appearance of erosion products and higher ionization modes of the argon [3], which are concentrated in the center of the plasma jet. Therefore, higher ionization modes were taken into account in the numerical MPD–codes and also a four fluid model, including either a nonreacting impurity component or a double ionized ion component with a nonequilibrium second level ionization reaction was developed for the theoretical instability investigations [27].

For a detailed investigation of the plasma parameters and conditions inside the MPD–thruster, a special designed DT7–thruster was built close to the DT2–geometry, with windows near the anode and in the throat area ( Fig. 5.7 ). Using a set–up of optical fibers, already

tested in the IRS plasma wind tunnel, in the near furture new investgations of the MPD-thrusters near onset conditions are planned.
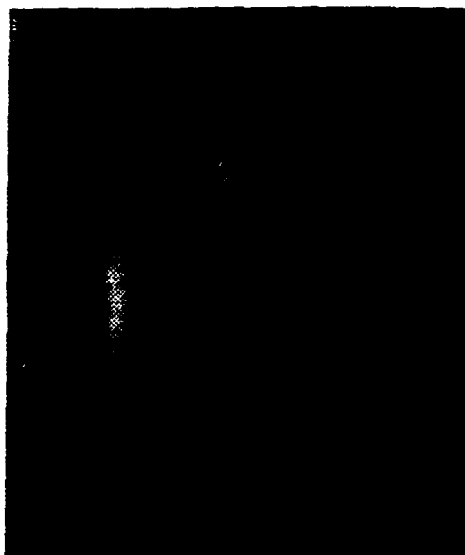


**Fig. 5.6: CCD-camera photographs at onset conditions of the nozzle type thrusters**
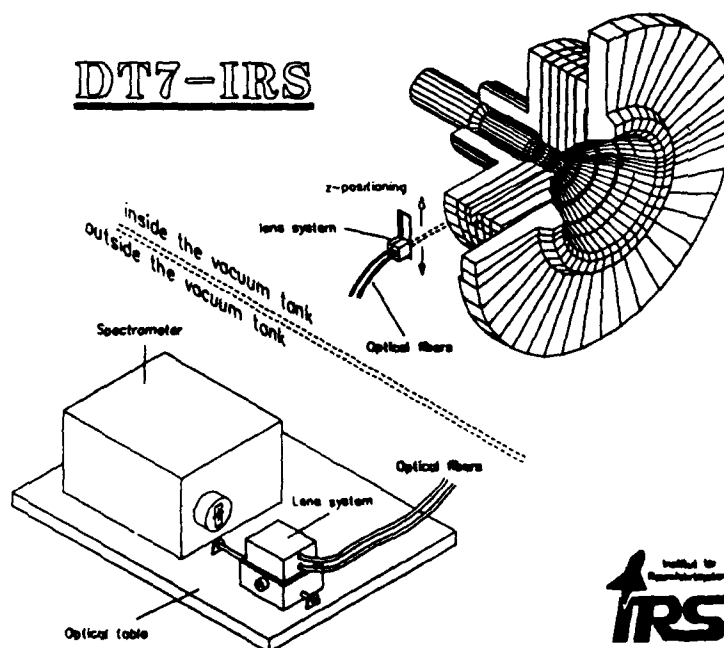


**Fig. 5.7: Planned optical measurements with the DT7-thruster**

As mentioned above, with the cylindrical thruster ZT3 no instabilities occur so far, although during the tests a correlation factor of $A = 8 \cdot 10^{10} A^2 s/kg$ was reached. Tests with lower mass flow rates at high current levels will be conducted in order to see, if or at which critical value $A_{crit}$ the pure cylindrical thruster becomes unstable. A comparison of the type one nozzle will hopefully give more insight to the so-called " Onset "- phenomenon.

## 6. Numerical Modeling of the Flow in MPD Accelerators

In order to gain a more thorough understanding of the investigated MPD-thrusters and for the optimization of these devices, numerical MPD-codes have been developed at the IRS (partially under grant AFOSR-86-0337 and AFOSR-91-0118).

A partly two-dimensional, time independent code for continuously running, nozzle type MPD-thrusters has already been described in the Progress Report of Grant AFOSR-89-0535 [11]. This code and all the other codes previously developed only consider the complete first stage ionization. The calculated results correspond very well with experimental results for operation parameters considering complete first stage ionization in the discharge area of an MPD-thruster. Calculations with higher current levels differ more from experimental results. Experimental investigations for the MPD thrusters at these high power values show second stage ionized argon III emission lines in the spectrum, in addition to the common argon lines, indicating that a numerical code ignoring higher stage ionization cannot supply satisfactory results. Therefore a new, two-dimensional axisymmetrical code was developed for an argon plasma propellant allowing ionization up to the third stage.

### 6.1 Two–Dimensional Modeling

The two–dimensional numerical code is based on a finite volume method for the gas dynamic flow calculations, the so called EUFLEX CODE [28], The Gauss–Seidel method for the electromagnetic discharge [29, 30] and the electron energy equation [31,32].

In addition to the geometry of the thruster, the code requires the mass flow rate and the electric current as input data, the heavy particles temperature and Mach number at the starting point and the boundary values of the electron temperature as an input from the experimental investigations. This yields the following results: flow, electron– and heavy particle temperature distribution, pressure distribution, velocity, Mach number distribution, magnetic field, current density distribution, and the electromagnetic and electrothermal thrust. Losses due to thruster surfaces and electrode fall voltages are not included in the numerical model.

#### 6.1.1 Discharge Code

In order to calculate the current distribution of the arc discharge, a two-dimensional computer code has been developed. Azimuthal current is neglected in the discharge code.

The basic equation for the discharge is the extended Ohm's law for plasmas:

$$\vec{j} = \sigma\left(\vec{E} + \vec{v} \times \vec{B}\right) - \frac{\omega_c \tau_c}{B}\left(\vec{j} \times \vec{B}\right) \tag{1}$$

Rewriting the Ohm's law by means of Maxwell's equations, one obtains a vector equation for the magnetic induction vector $\vec{B}$ in the form

$$0 = \frac{1}{\mu_0}\left(\nabla \times \left(\frac{1}{\sigma}\nabla \times \vec{B}\right) - \left(\nabla \times \left(\vec{v} \times \vec{B}\right)\right)\right) + \frac{1}{\mu_0}\left(\nabla \times \left(\beta\left(\nabla \times \vec{B}\right) \times \vec{B}\right)\right) \tag{2}$$

with

$$\beta = \frac{\omega\tau}{B_\theta\sigma} = \frac{1}{en_e} \tag{3}$$

With the Jacobian J of the transformation from cylindrical to the curvilinear coordinates:

$$J = \frac{1}{\dfrac{\partial z}{\partial \xi}\dfrac{\partial r}{\partial \eta} - \dfrac{\partial z}{\partial \eta}\dfrac{\partial r}{\partial \xi}} \tag{4}$$

where the matrices are formed in terms of the derivatives of the cylindrical coordinates as follows:

$$\xi_z = J\frac{\partial r}{\partial \eta}, \qquad \eta_z = -J\frac{\partial r}{\partial \xi}, \qquad \xi_r = -J\frac{\partial z}{\partial \eta}, \qquad \eta_r = J\frac{\partial z}{\partial \xi} \tag{5}$$

where the convention $\xi_z = \dfrac{\partial z}{\partial \xi}$, etc. is used.

The equation (2) follows with a stream function $\Psi = rB_\theta$ the elliptical, partial differential equation of 2nd order

$$
\begin{aligned}
&\frac{\partial^2\psi}{\partial\xi^2}(\xi_z^2 + \xi_r^2) + 2\frac{\partial^2\psi}{\partial\xi\partial\eta}(\xi_z\eta_z + \xi_r\eta_r) + \frac{\partial^2\psi}{\partial\eta^2}(\eta_z^2 + \eta_r^2) + \frac{\partial\psi}{\partial\xi}\left\{\xi_z\frac{\partial\xi_z}{\partial\xi} + \eta_z\frac{\partial\xi_z}{\partial\eta} + \xi_r\frac{\partial\xi_r}{\partial\xi} + \eta_r\frac{\partial\xi_r}{\partial\eta}\right.\\[4pt]
&+ \xi_z\left[-\frac{1}{\sigma}\left(\xi_z\frac{\partial\sigma}{\partial\xi} + \eta_z\frac{\partial\sigma}{\partial\eta}\right) - \frac{\sigma\Psi}{R}\left(\xi_r\frac{\partial\beta}{\partial\xi} + \eta_r\frac{\partial\beta}{\partial\eta}\right) + \frac{2\sigma\beta\Psi}{R^2} - \sigma\mu_0 u\right]\\[4pt]
&\left.+ \xi_r\left[-\frac{1}{R} - \frac{1}{\sigma}\left(\xi_r\frac{\partial\sigma}{\partial\xi} + \eta_r\frac{\partial\sigma}{\partial\eta}\right) + \frac{\sigma\Psi}{R}\left(\xi_z\frac{\partial\beta}{\partial\xi} + \eta_z\frac{\partial\beta}{\partial\eta}\right) - \sigma\mu_0 v\right]\right\}\\[4pt]
&+ \frac{\partial\Psi}{\partial\eta}\left\{\xi_z\frac{\partial\eta_z}{\partial\xi} + \eta_z\frac{\partial\eta_z}{\partial\eta} + \xi_r\frac{\partial\eta_r}{\partial\xi} + \eta_r\frac{\partial\eta_r}{\partial\eta} + \eta_z\left[-\frac{1}{\sigma}\left(\xi_z\frac{\partial\sigma}{\partial\xi} + \eta_z\frac{\partial\sigma}{\partial\eta}\right)\right.\right. \quad (6)\\[4pt]
&- \frac{\sigma\Psi}{R}\left(\xi_r\frac{\partial\beta}{\partial\xi} + \eta_r\frac{\partial\beta}{\partial\eta}\right) + \frac{2\sigma\beta\Psi}{R^2} - \sigma\mu_0 u\bigg] + \eta_r\left[-\frac{1}{R} - \frac{1}{\sigma}\left(\xi_r\frac{\partial\sigma}{\partial\xi} + \eta_r\frac{\partial\sigma}{\partial\eta}\right)\right.\\[4pt]
&\left.\left.+ \frac{\sigma\Psi}{R}\left(\xi_z\frac{\partial\beta}{\partial\xi} + \eta_z\frac{\partial\beta}{\partial\eta}\right) - \sigma\mu_0 v\right]\right\} + \sigma\mu_0\Psi\left(\frac{v}{R} - \frac{\partial U}{\partial\xi} - \frac{\partial V}{\partial\eta}\right) = 0
\end{aligned}
$$

with U and V as the contravariant velocities

$$U = \xi_z u + \xi_r v \qquad\qquad V = \eta_z u + \eta_r v \tag{7}$$

The function $\Psi(r,z) = $ const now represents a current contour line, since $B = B_\theta$ is proportional to $\dfrac{I(r)}{R}$, where $I(r)$ is the electric current carried through a cross sectional area of $\pi r^2$. The proper boundary conditions for $\Psi$ follow from the geometry of the thruster walls and electrodes. At the insulator inside the thruster and at the inflow boundary $\Psi$ is set to $-\dfrac{\mu_0}{2\pi} I$. For the electrodes the electric field is assumed to be normal to the surfaces $\vec{E}\cdot\vec{t} = 0$. In accordance with the grid in Fig. 3, it is equal to $E_\xi = 0$, and it follows to:

$$\frac{\partial\Psi}{\partial\eta}\left[\frac{\beta\Psi}{R}(\xi_r\eta_r - \xi_z\eta_z) + \frac{1}{\sigma}(\xi_z\eta_r - \xi_r\eta_z)\right] + \frac{\partial\Psi}{\partial\xi}\frac{\beta\Psi}{R}(\xi_r^2 - \xi_z^2) + (\xi_r u - \xi_z v) \tag{8}$$

At the other boundary sections and at the symmetry axis $\Psi$ is set to 0.

### 6.1.1.1 Ionization of an Argon Plasma

Due to the higher mobility of the electrons, the ionization of the argon plasma in MPD–thrusters is dominated by the electron temperature. The Saha equation results into the equation for the different ionization levels.

$$\frac{n_{i+1}}{n_i} p_e = \frac{g_{i+1}}{g_i} 2 \frac{(2\pi m_e)^{3/2}(kT_e)^{5/2}}{h^3} e^{-\frac{\varepsilon_i}{kT_e}} \tag{9}$$

Here $p_e$ is the partial pressure of the electrons, $n_i$ the number densities, $g_i$ the weighting factor taking into account the degenerated states and $\varepsilon_i$ the ionization energy of the ionization level $i$.

The sum of the partial pressures of all plasma components yields the total pressure

$$p = \sum_{v(=e)} n_v k\, T_v \tag{10}$$

and the neutrality of charge

$$n_e = \sum_{v(=e)} z_v n_v \tag{11}$$

considering the higher ionization modes up to the third ionization level the eqations 9 - 11 yield a fourth order polynom for the electron density. In equation 10, $T_v$ represents the electron temperature $T_e$ and the heavy particles temperature, which for all heavy particles is equal to $T_{tr}$. In equation 11, $z_v$ stands for the charge number.

$$a_1 n_e^4 + a_2 n_e^3 + a_3 n_e^2 + a_4 n_e + a_5 = 0 \tag{12}$$

with
$$a_1 = \frac{h^3 T_{tr}}{12\,(2\pi m_e kT_e)^{3/2}}\, e^{\frac{\varepsilon_1}{kT_e}}$$

$$a_2 = T_e + T_{tr}$$

$$a_3 = \frac{3(2\pi m_e kT_e)^{3/2}\,(2T_e + T_{tr})}{h^3 T_{tr}}\, e^{-\frac{\varepsilon_2}{kT_e}} - \frac{p}{k}$$

$$a_4 = \frac{3(2\pi m_e kT_e)^{3/2}}{h^3 T_{tr}}\, e^{-\frac{\varepsilon_2}{kT_e}} \left( \frac{(2\pi m_e kT_e)^{3/2}\,(3T_e + T_{tr})}{h^3 T_{tr}}\, e^{-\frac{\varepsilon_3}{kT_e} - \frac{2p}{k}} \right)$$

$$a_5 = \frac{3p}{k}\, \frac{3(2\pi m_e kT_e)^{3/2}}{h^3 T_{tr}}\, e^{-\frac{\varepsilon_2}{kT_e}}\, \frac{(2\pi m_e kT_e)^{3/2}}{h^3 T_{tr}}\, e^{-\frac{\varepsilon_3}{kT_e}}$$

The eqation for the electron density is solved by a Newton iteration. With this electron density the other partial densities like the argon atoms and the different ions are determined.

The electric conductivity of a plasma is determined by [33]:

$$\sigma = \frac{3}{8}\sqrt{\frac{\pi}{2}}\, \frac{e^2 n_e}{\sum_{v(=e)} n_n Q_{ev}\sqrt{m_{ev}kT_{ev}}} \tag{13}$$

Here $m_{ev} = \dfrac{m_e m_v}{m_e + m_v}$ is the reduced mass and $T_{ev} = \dfrac{m_v T_e + m_e T_v}{m_v + m_e}$ the reduced temperature.
With respect to the different ionized levels the Gvosdover cross sections follows by [34]:

$$Q_{ei} = \frac{\pi}{4}\left(\frac{z_i e^2}{4\pi\varepsilon_0 k T_e}\right)^2 \ln\left(144\pi^2 \frac{\varepsilon_0^3 T_e^3 k}{n_e e^6 (z_i^2(|z_i|+1))}\right) \tag{14}$$

For $Q_{ev}$ being the cross section between electrons and atoms in equation 13 the Ramsauer cross section is used [35]. From these eqations it is obvious that the high ionization levels have a strong effect on the electric conductivity.
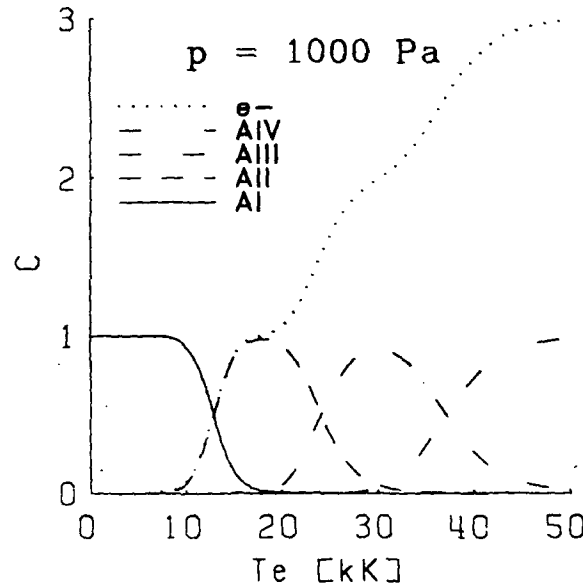


Fig. 6.1: Concentration of an argon plasma.

For an electron temperature up to 50 kK and a constant pressure of 1000 Pa in Fig. 6.1, a typical concentration distribution with respect to the sum of heavy particles is presented.

## 6.2 Electron Energy Equation

In order to determine the electron temperature, the electron energy equation is developed from the Boltzmann equation. The electron temperature has a strong effect on the electrical and thermal conductivity as well as on the electron density, which again influences the discharge pattern. Therefore, a two-dimensional code for the electron temperature distribution, corresponding to the two-dimensional discharge code, was written.

The electron temperature distribution is determined by the energy equation for the electron component.

$$\nabla(\lambda_e \nabla T_e) + \frac{5}{2}\frac{k}{e}\vec{j}\,\nabla T_e - \frac{\vec{j}^2}{\sigma} - \sum_v n_v n_e \alpha_{ev}(T_e - T_{tr}) - \varepsilon_{ion}\frac{\partial n_e}{\partial t}\Big|_{rct} \tag{15}$$

The first term on the left hand side represents the heat flux in the electron gas, and the second term gives the convective heat flux of the electron gas due to the current transport. The

37

energy input due to ohmic heating is represented by the first term on the right hand side. The sum of losses due to the energy transfer from the electron gas to the heavy particles gas is calculated by the second term on the right hand side. The reaction losses are given by the last term, where $\varepsilon_{ion}$ is given by Unsöld [36].

The heat transfer coefficient $\alpha_{ev}$ and the thermal conductivity $\lambda_e$ depend on the electron temperature [31, 33], where the heat transfer coefficient is

$$\alpha_{ev} = \frac{8\sqrt{2}}{\sqrt{\pi}} Q_{ev} \sqrt{\mu_{ev} k T_{ev}} \; \frac{k}{m_e + m_v} \tag{16}$$

and the thermal conductivity:

$$\lambda_e = \frac{15}{8} \sqrt{\frac{\pi}{2}} \; \frac{n_e k^2 T_e}{\displaystyle\sum_{v(=e)} n_v Q_{ev}\sqrt{m_v k T_v} \frac{m_e}{m_e + m_v}} \tag{17}$$

where $Q_{ee}$ is the Gvosdover cross section from equation 14 for a charge number $z_i = -1$. For $Q_{ev}$ being the cross section between the electrons and the different ionized ions, also the Gvosdover cross section from equation 14 is used. For $Q_{ev}$ being the cross section between electrons and the atoms, the Ramsauer cross section is used.

With respect to the rotational symmetry, equation 15 results in the following elliptical, partial differential equation of 2nd order:

$$(\eta_r^2 + \eta_z^2) \frac{\partial^2 T_e}{\partial \xi^2} + (\xi_z^2 + \xi_r^2) \frac{\partial^2 T_e}{\partial \eta^2} + 2(\xi_z \eta_z + \xi_r \eta_r) \frac{\partial^2 T_e}{\partial \xi \partial \eta} +$$

$$\frac{J^2}{4\lambda_{ec} T_e^{5/2}} \left[ \sum_v n_e n_v \alpha_e (T_{tr} - T_e) + \frac{\vec{J}^2}{\sigma} - \varepsilon_{ion} \cdot \left( u \frac{\partial n_{e,rct}}{\partial \xi} + v \frac{\partial n_{e,rct}}{\partial \eta} \right) - \tag{18} \right.$$

$$\frac{n_e k T_e}{J} ( {}^r\eta u_\xi - r_\xi u_\eta + z_\xi v_\eta - z_\eta v_\xi ) - \frac{3 n_e k}{2J} \left( u r_\eta \frac{\partial T_e}{\partial \xi} - u r_\xi \frac{\partial T_e}{\partial \eta} + v z_\xi \frac{\partial T_e}{\partial \eta} - v z_\eta \frac{\partial T_e}{\partial \xi} \right) - $$

$$b \frac{\partial T_e}{\partial \eta} - c \frac{\partial T_e}{\partial \xi} = 0$$

Here $\xi$ and $\eta$ indicate the partial differentiation to the curvilinear $\xi$- and $\eta$-directions. The terms $a$ and $b$ are metric terms and $J$ is the Jacobian of the transformation.

At the outflow boundary $T_e$ is set to a value in accordance with measurements[37]. Inside, the solid bodies of the thruster are treated as thermal insulators; therefore $\nabla T_e \cdot \vec{n} = 0$, where $\vec{n}$ is the normal vector of the surfaces. Due to the axial symmetry, $\partial T_e / \partial r = 0$ on the axis. At the inflow boundary $T_e$ is set to a constant value of 7000 K in accordance with the measurements.

### 6.3 Flow Field Code

For the description of the two-dimensional, axisymmetric flow, the following nonlinear hyperbolic system of differential equations with curvilinear, cylindrical coordinates is used.

$$\frac{\partial}{\partial t}\vec{q} + \frac{\partial}{\partial \xi}\vec{F}(\vec{q}) + \frac{\partial}{\partial \eta}\vec{G}(\vec{q}) + \vec{H}(\vec{q}) = 0 \qquad (19)$$

The indices $t$, $\xi$, $\eta$ indicate the partial differentiation with respect to time and to the $\xi$- and $\eta$-directions.

The first three terms are used in the usual fluid dynamic manner, where $\vec{q}$ is the flow variables vector and $\vec{F}$ and $\vec{H}$ are the spatial derivatives vectors[28]. The source vector $\vec{H}$ is developed to:

$$\vec{H}(\vec{q}) = \begin{bmatrix} \rho v/R \\[2mm] \rho uv/R + \frac{\partial}{\partial \xi}\left\{\mu\left[2\frac{\partial U}{\partial \xi} + \left(\frac{\partial V}{\partial \xi} + \frac{\partial U}{\partial \eta}\right)\right]\right\} + j_\eta B_\theta \\[2mm] \rho v^2/R + \frac{\partial}{\partial \eta}\left\{\mu\left[2\frac{\partial V}{\partial \eta} + \left(\frac{\partial U}{\partial \eta} + \frac{\partial V}{\partial \xi}\right)\right]\right\} + j_\xi B_\theta \\[2mm] (p + e_s)v/R + \nabla\vec{q}_s - \sum_v n_v n_e \alpha_{ev}(T_{tr} - T_e) \end{bmatrix}$$

The first terms in the source vector transform the plane two–dimensional set of equations into a cylindrical calculation. The first additional terms in the impulse equations represent the stress tensor of the plasma flow, where the viscosity coefficient $\mu$ is given by:

$$\mu = \frac{3}{8}\sqrt{\frac{\pi}{2}} \sum_l \frac{m_l n_l k T_{tr}}{\sum_{v(=l)} n_v Q_{lv}\sqrt{m_v k T_v}\frac{m_l}{m_l + m_v}} \qquad (20)$$

The last terms in the impulse equations represent the $\vec{j} \times \vec{B}$ forces from the electromagnetic field. In the energy eqation the second source vector term $\vec{q}_s$ represents the heat flux vector due to the heavy particles of the MPD flow, which is given by:

$$\vec{q}_s = \sum_l -\lambda_l\left(\frac{1}{2}\frac{T_{tr}}{n_l}\nabla n_l + \nabla T_{tr}\right) \qquad (21)$$

Here the heat conductivity coefficients are given by:

$$\lambda_l = \frac{15}{8}\sqrt{\frac{\pi}{2}} \frac{n_l k^2 T_{tr}}{\sum_{v(=l)} n_v Q_{lv}\sqrt{m_v k T_v}\frac{m_l}{m_l + m_v}} \qquad (22)$$

The transfer of Joules heat is contained in the temperature compensation between the electron and the rotational temperature, which is represented by $\sum_v n_v n_e \alpha_{ev}(T_e - T_{tr})$ in the equation of energy conservation.

The transport coefficients are derived in a similar manner as in [38], and more detailed derivations for the coefficients are described in [33]. The cross sections $Q_{lv}$ for all coefficients are taken from the references [34, 35].

## 6.4. Solution of the Equation Systems

The three models described in subsection 6.1-6.3 are solved in the following manner:

For a given flow field, the discharge equation and hence the electron temperature is determined. With these results the flow field equations are calculated. This new flow field and the new distribution of the electron temperature are taken to calculate the discharge equation, and so on. These iteration steps are repeated until the calculated data, such as electron temperature distribution, current distribution and the heavy particles flow field have reached numerical equilibrium.

The extended Euler equations which determine the heavy particles flow, are solved by the finite volume method EUFLEX [28]. The two nonlinear, elliptical, partial differential equations 6 and 18 are solved with a Gauss-Seidel finite difference method.

## 6.5 Numerical Results

The calculation grid of the cylindrical thruster ZT2 should be very fine, since strong gradients occur all over in the investigated domain. In Fig. 6.2 only each second point in both directions of the grid is shown, which was used for the calculations presented in this chapter.
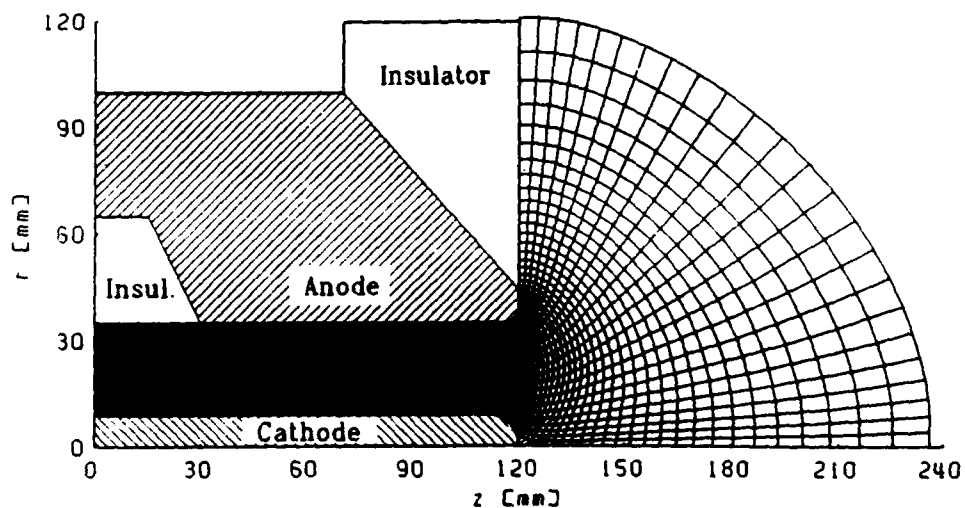


**Fig. 6.2: Calculation grid of the ZT2 thruster.**

The results which are presented in this chapter were calculated for the ZT2 self-field MPD thruster at steady state conditions. The ZT2-thruster has the same geometry as the ZT1 one, but only one insulator segment. The flow inlet boundary conditions were iterated to coincide with an experimentally obtained cold gas thrust of 1 N at a mass flow rate of 2 g/s. For a given current of 8 kA the computation yields the current density distribution, as illustrated in

40

Fig. 6.3. The calculated current contour distribution corresponds with that obtained for a continuing mode, if the cathode is hot glowing and is emitting sufficient electrons along its complete length.
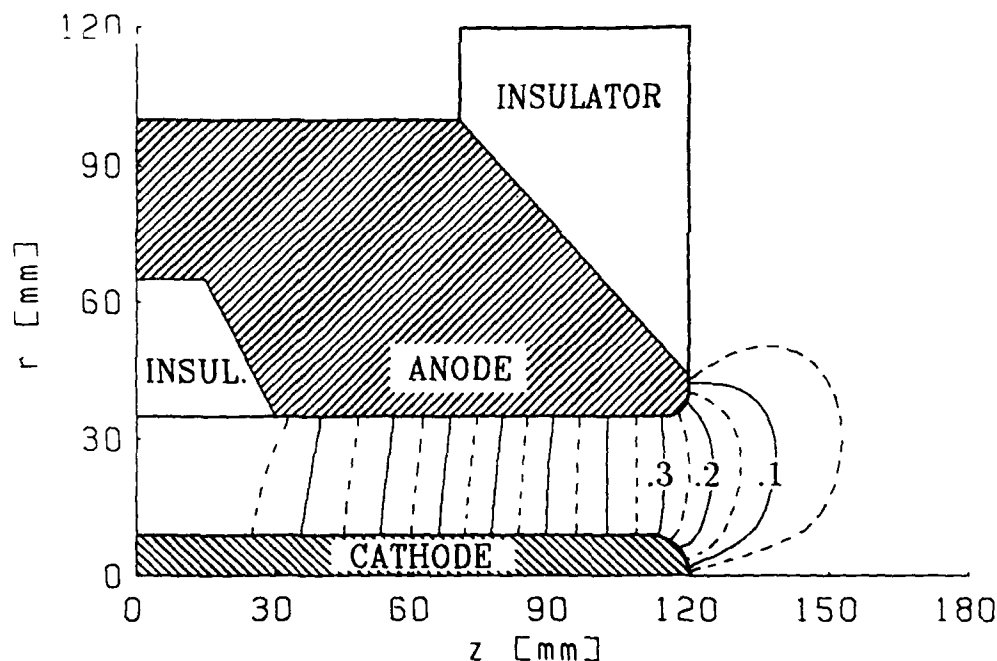


**Fig. 6.3: Calculated current contour lines.**

Figure 6.4 shows the ionization distribution of the argon plasma up to the 3rd ionization level. This ionization number shown here is calculated like the electron concentration in Fig. 6.1 with respect to the sum of the heavy particles to $\alpha = n_e / \sum_{v(\ge e)} n_v$. The ionization grows in the first 30 mm after the inflow border up to 1. In the rest of the inside area and in a big part of the presented outside area there is approximately singulary fully ionized plasma. Going in front of the cathode to the symmetry axis, the ionization increases to the maximum value of 3. That indicates relatively low pressure and a high temperature there. Outside the thruster in radial direction out of the symmetry axis the ionization decreases slowly.

The earlier approximation in the calculation model of up to singulary fully ionized plasma was quite good, since the biggest calculated area is lower or roughly singulary fully ionized.

The electron temperature distribution within and outside the thruster is shown for a calculation taking into account the first fully ionization (a) and for a calculation up to the third ionization level (b) in Fig. 6.5. The maximum electron temperature value for both cases is on the tip of the cathode on the symmetry axis, but there is also a small increase at the beginning of the anode and a remarkable increase of the electron temperature at the end of the anode outside the thruster. The electron temperature distribution doesn't differ very much in both calculations. The biggest difference of the temperature values is at the maximum temperatures.

The calculation up to the 3rd ionization level yields a 2.6 kK lower electron temperature there, due to the energy consuming higher level ionization.

41
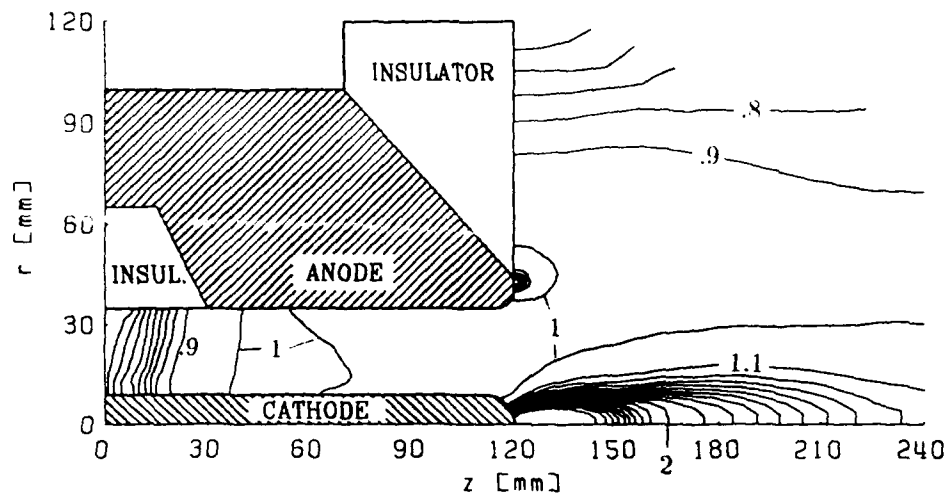
Fig. 6.4: Ionization distribution.
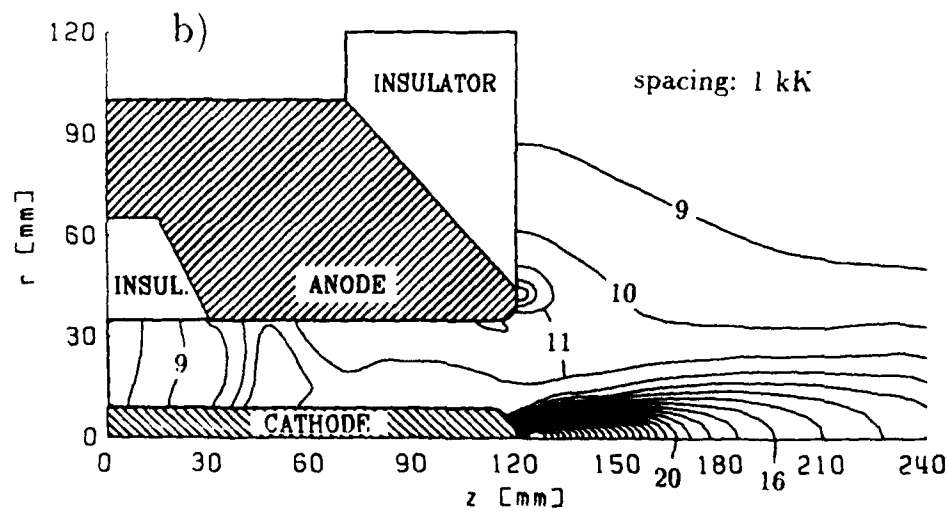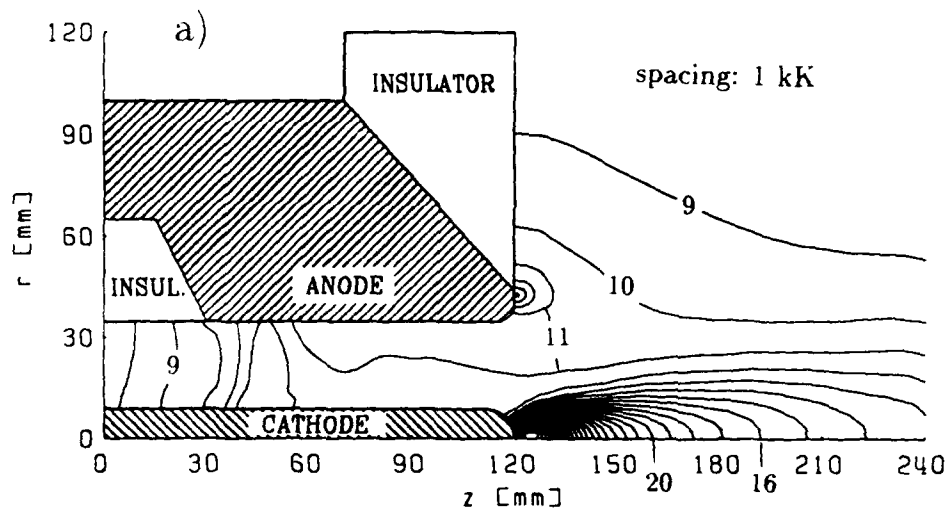


Fig. 6.5: Electron temperature contours up to the 1st (a) and up to the 3rd (b) ionization given in [kK].

42
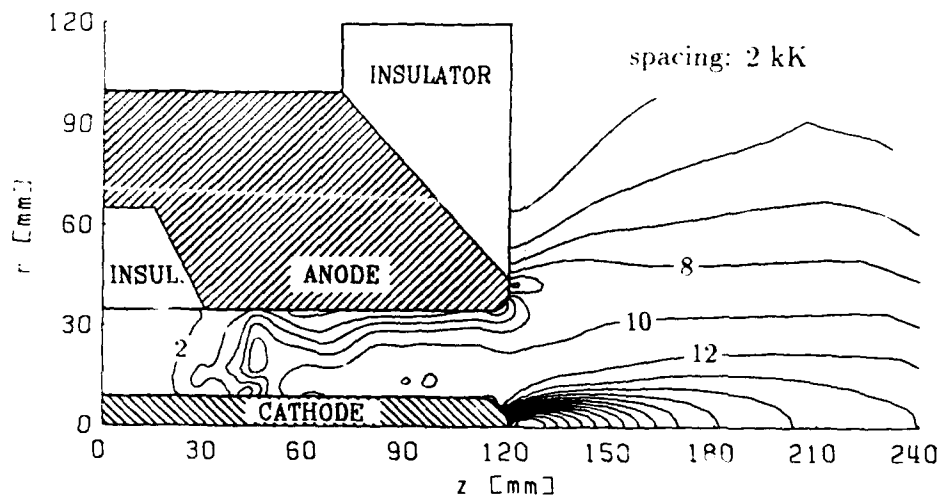
**Fig. 6.6: Heavy particles temperature contours in [kK].**

The heavy particle temperature distribution within and outside the thruster is shown in Fig. 6.6. The maximum temperature value of the heavy particles is also in front of the cathode on the symmetry axis. The increase of the heavy particles temperature at the ends of the anode is not as strong as for the electron temperature.

The density map (Fig. 6.7) illustrates the expansion flow with the flow described in section 6.3, where the relatively low pinch effect was taken into account.
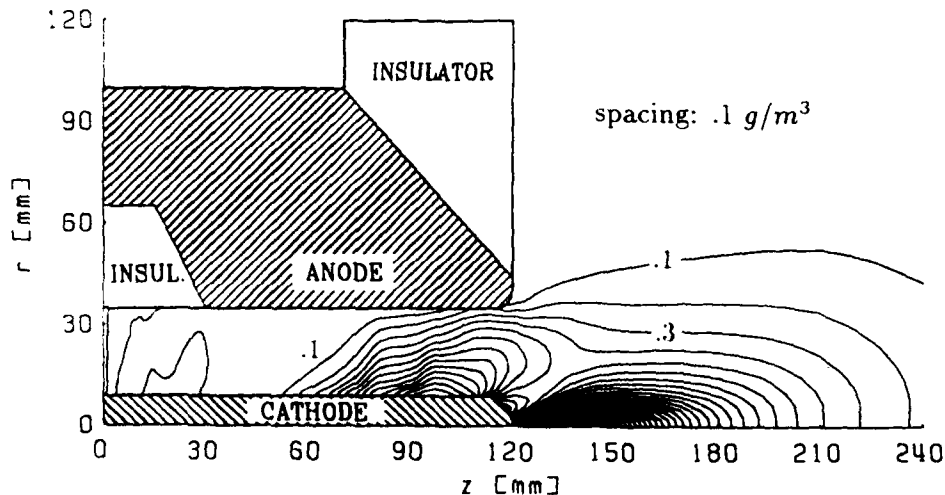


**Fig. 6.7: Density distribution.**

The completion of the velocity distribution to the temperatures and density distribution is shown in Fig. 6.8 as a vector graph. It shows a high increase from the inflow boundary downstream. The radial velocity components inside the channel are quite small, which is an indication for a relatively low pinch effect there.

43
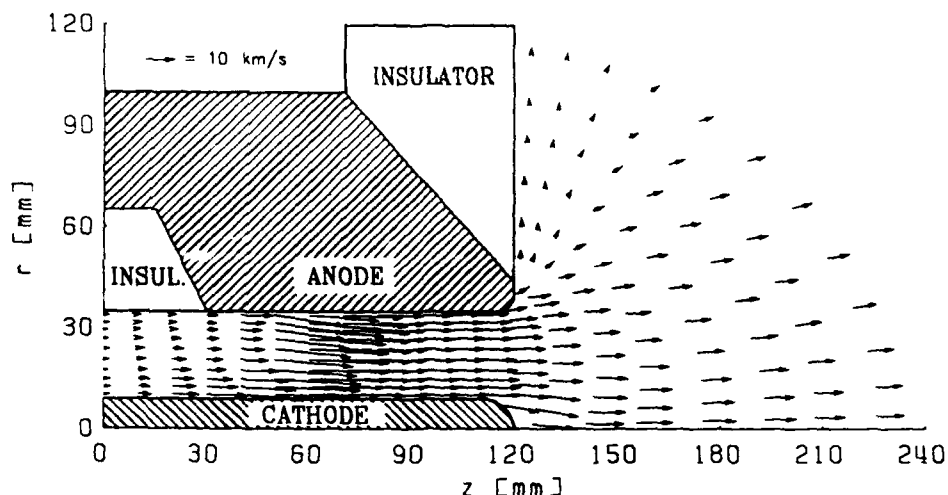
**Fig. 6.8: Velocity vector distribution.**

According to the flow conditions and the known electromagnetic force configuration, the thrust can be calculated. The thrust of an MPD thruster is the sum of all gas dynamic surface forces and the electromagnetic volume forces. Hence it is

$$\overrightarrow{T} = \int_{A_S}\left(\rho\overleftrightarrow{vv} + \overleftrightarrow{P}\right)\cdot d\overrightarrow{A} - \int_{V_C}\overrightarrow{j}\times\overrightarrow{B}\,dV \tag{23}$$

where $A_S$ represents the surface of all internal walls and $V_C$ is the current carrying plasma volume. For the case presented here the total thrust was calculated as 15 N. This includes 13 N electromagnetic thrust and 1 N cold gas thrust.

## 6.6 Comparison with experiments

As can be seen in Fig. 3.1 the anode of the ZT2 thruster is divided into three segments of 30 mm width. The current in each of the segments is measured separately during the experiment.

| | Percentual Current Fraction into Anode Segments | | | Voltage |
|---|---|---|---|---|
| | Anode 1 | Anode 2 | Anode 3 | |
| Thy. 1 | 50 | 27 | 23 | 16V |
| Thy.3 | 49 | 28 | 23 | 16V |
| Exp. | 44 | 31 | 25 | 20V |

Table 6.1: Comparison of numerical (at 8000 A) and experimental (at 7700 A) results.

The measured data of Tab. 6.1 agree well with the numerical results of Fig. 6.3. For example, the experimentally determined current percentage are 44% of the total for the downstream anode segment, 31% for the middle, and 25% for the upstream section. This must be compared with the theoretical percentage of 50%, 27% and 23% for the calculation up to the 1st ionization (Thy.1) and with 49%, 28%, and 23% for the calculation up to the 3rd ionization (Thy.3). The measured voltage drop was 20 V, whereas the calculation gave a somewhat

44

lower figure of 16 V. Since the numerical model does not include electrode fall voltages, the theoretical number matches the experiment quiet well.

## 6.7 Conclusions

The code described in this report was developed and tested in order to gain a more profound understanding of the fundamental processes occuring in MPD-thrusters and in order to end up with reliable design criteria and predict thruster performances under various conditions.

The extension up to the 3rd ionization level leads to better agreement with experiments at high specific impulses. With the curvilinear grid, the code permits an improved simulation of geometry dependencies.

In a later research period nozzle type thruster designs will also be investigated with the code at high specific impulse values. For these calculations the consideration of the higher ionization modes is more important than for the calculation presented in this paper. In addition, the change to a Navier-Stokes code for the flow field calculation is planned.

## 7. List of Reports and Publications

During the period of the research grant the following reports have been published:

M. Auweter-Kurtz, H. Kurtz, H. Schrade, C. Sleziona," Numerical Modeling of the Flow Discharge in MPD-Thrusters ", Journal of Propulsion and Power, Vol. 5, No. 1, pp. 49-55, 1989

M. Auweter-Kurtz, H. Kurtz, W. Merke, H. Schrade, C. Sleziona, Th. Wegmann," High Power Steady State Thrusters ", IRS-90-P4, Final report Grant AFOSR-88-0325, Institut für Raumfahrtsysteme, University of Stuttgart, 1990

Th. Wegmann, M. Auweter-Kurtz, H Kurtz, W. Merke, O Loesener, H Schrade," Steady State High Power MPD Thrusters ", AIAA-90-2555, 21st IEPC, Orlando, Fl, 1990

M. Auweter-Kurtz, H. Habiger, S. Laure, E. Messerschmid, A. Schönemann," Experimental Investigations of MPD Devices Used as Reentry test Plasma Sources ", AIAA-90-2570, 21st IEPC, Orlando, Florida, 1990

C. Sleziona, M. Auweter-Kurtz, H. Schrade," Numerical Evaluation of MPD Thrusters", AIAA-90-2602, 21st IEPC, Orlando, Florida, 1990

C. Sleziona, M. Auweter-Kurtz, H. Schrade, Th. Wegmann,"Comparison of Numerical and Experimental Investigations of Nozzle Type MPD-Accelerators", AIAA-90-2663, 21st IEPC, Orlando, Fl, 1990

H. Wagner, M. Auweter-Kurtz, H. Kaeppeler, Th. Roesgen, E. Messerschmid," Gradient Driven Instabilities in Stationary MPD Thruster Flows", AIAA-90-2603, 21st IEPC, Orlando, 1990

M. Auweter-Kurtz, E. Messerschmid," Plasma Accelerator Activities at the IRS", AIAA-90-2659, 21st IEPC, Orlando, Florida, 1990

M. Auweter-Kurtz, B. Glocker, H. Kurtz, O. Loesener, H. Schrade, N. Tubanos, Th. Wegmann," Cathode Phenomena in Plasma Thrusters", AIAA-90-2662, 21st IEPC, Orlando, Florida, 1990

J. Polk, A. Kelly, R. Jahn, H. Kurtz, H. Schrade, M. Auweter-Kurtz," Mechanisms of Hot Cathode Erosion in MPD Thrusters ", AIAA-90-2673, 21st IEPC, Orlando, Florida, 1990

C. Sleziona, M. Auweter-Kurtz, H. Schrade," Computation of MPD Flows and Comparison with Experimental Results ", Second World Congress on Computational Mechanics, Stuttgart, August 1990

M. Auweter-Kurtz, H. Kurtz, H. Schrade, C. Sleziona, Th. Wegmann," High Power Steady State MPD Thrusters", IRS-91-P4, Institut für Raumfahrtsysteme, University of Stuttgart, 1991

P. Sleziona, M. Auweter-Kurtz, H. Schrade," MPD Thruster Calculation Considering High Ionization Modes", IEPC-91-087, 22nd IEPC, Viareggio, 1991

H.O. Schrade, Th. Wegmann, Th. Rösgen, "The Onset Phenomena Explained by Run-Away Joule heating", IEPC-91-022, 22nd IEPC, Viareggio, 1991

H. Wagner, M. Auweter-Kurtz, H. Kaeppeler, E. Messerschmid, " Gradient Influenced Space Charge Instabilities in MPD Thrusters ", IEPC-91-101, 22nd IEPC, Viareggio, 1991

H. Kaeppeler," Basic Equation and Llements of the Dispersion relation for a Four-Fluid Formalism of Magneto-Plasmadynamics with Non-Equilibrium Ionization ", IEPC-91-059, 22nd IEPC, Viareggio, 1991

Th. Wegmann, M. Auweter-Kurtz, H. Habiger, H. Kurtz, H. Schrade," Experimental Investigation of Steady State High Power MPD Thrusters ", AIAA-92-3464, 28th Joint Propulsion Conference, Nashville, 1992

**Diploma and Student Thesis at the IRS**

W. Mayer," Numerische Berchnung der Stömung im zylindrischen MPD-Triebwerk mit einem Finiten-Volumen-Verfahren", IRS-89-S1, Diplomathesis, 1989

U. Fuchs," Gekuppelte Berechnung von zylindrisches MPD-Triebwerken ", IRS-89-, Diplomathesis, 1989

H-M. Gerhard," 2-Dimensionale Strömungsberechnung eines düsenförmigen MPD-Triebwerkes ", IRS-89-, Diplomathesis, 1989

A. Renner," Berechnung von Plasmatriebwerken mit unterschiedlicher Düsengeometrie", IRS-90-S12, Student thesis, 1990

R. Müller," Gescwindigkeitsmessungen in Triebwerksplasmen", IRS-90-S20, Student thesis, 1990

H. Früholz," Experimente zur Optimierung der Betriebscharakteristiken von düsenförmigen MPD Antrieben", IRS-90-S18, Student thesis, 1990

S. Oesterle," Kathodenerosionsuntersuchungen an MPD-Triebwerken", IRS-90-S21, Student thesis, 1990

O. Preising," Plasmageschwindigkeitsmessungen mit einem Fabry-Perot-Interferometer", IRS-92-S3, Student thesis, 1992

Th. Stöckle," Methoden der Geschwindigkeitsmessung mit elektrostatischen Sonden", IRS-92-S5, Student thesis, 1992

M. Vayhinger," Stömungslinienmessungen mit elektrostatischen Sonden", IRS-92-S6, Student thesis, 1992

P. Kungl," Temperatur und Dichtemessungen mit elektrostatischen Sonden", IRS-92-S9, Student thesis, 1992

J. Kleinschmidt," Berechnungen von MPD-Triebwerken unter Berücksichtigung eines variablen Ionisationsgrades", IRS-92-S11, Student thesis, 1992

**Dissertation at the IRS**

P.C. Sleziona," Numerische Analyse der Strömungsvorgänge in magnetoplasmadynamischen Raumfahrtantrieben, Dissertation, Stuttgart, 1992

## 8. References

[1] M. Auweter-Kurtz," Lichtbogenantriebe für Weltraumaufgaben", B.G. Teubner Verlag, Stuttgart, 1992

[2] P.C. Sleziona, M. Auweter-Kurtz, H.O. Schrade, Th. Wegmann,"Comparison of Numerical and Experimental Investigations of MPD-Accel. : : ", AIAA-90-2663, 21st IEPC, Orlando, Fl, 1990

[3] Th. Wegmann, M. Auweter-Kurtz, H.L. Kurtz, W. Merke, O.R. Loesener, H.O. Schrade,"Steady State High Power MPD Thrusters", AIAA-90-2555, 21st IEPC, Orlando, Fl, 1990

[4] H.L. Kurtz, M. Auweter-Kurtz, H.O. Schrade," Optimization of Electric Propulsion Systems Considering Specific Power as Function of Specific Impulse",Journal of Propulsion and Power, Vol. 4, No. 6, pp 512-519, 1988

[5] J. Gilland," NEP Mission Sensitivities", MPD Thruster Technology Workshop, Washington, DC, May 1991

[6] M. Auweter-Kurtz,H. Kurtz, W. Merke, H. Schrade, C. Sleziona, Th. Wegmann,"High Power Steady State MPD Thrusters", IR-S-90-P4, Final Report Grant AFOSR-88-0325, Institut für Raumfahrtsysteme, University Stuttgart, 1990

[7] H. Schrade, M. Auweter-Kurtz, H. Kurtz, W. Merke, C. Sleziona," Plasma Thruster Developement", IRS-87-P10, Final Report Grant AFOSR-84-0394, Institut für Raumfahrtsysteme, University Stuttgart, 1987+

[8] M. Auweter-Kurtz, H. Kurtz, W. Merke, H. Schrade, C. Sleziona,"Self-field MPD Thruster Investigations", IRS-88-P10, Final Report ONR Grant No. N 00014-87-G-0119, Institut für Raumfahrtsysteme, University Stuttgart, 1988

[9] H.O. Schrade, H.L. Kurtz, P.C. Sleziona, Th. Wegmann,"Basic Processes of Plasma Propulsion", Final Scientific Report Grant AFOSR-91-0118, Institut für Raumfahrtsysteme, University Stuttgart, 1992

[10]H. Maecker," Plasmaströmungen in Lichtbögen infloge eigenmagnetischer Kompression" Zeitschrift für Physik, Vol. 141, p198, 1955

[11]M. Auweter-Kurtz, H. Kurtz, H. Schrade, C. Sleziona, Th. Wegmann,"High Power Steady State MPD Thrusters" IRS-91-P4, Progress Report Grant AFOSR-89-0535, February 1991

[12]F. Chen, "Plasma Diagnostic Techniques", ed. by Huddlestone and Leonard, 1965

[13]J.G. Laframboise, "UTIAS-Report No. 100", University of Toronto, 1966

[14]J.W. Swift, M.J.R. Schawr, "Electric Probes for Plasma Diagnostics", Ilille Book LTD., London 1970

[15]F. Maissenhälder, W. Mayerhofer , "Jet Diagnostics of a Self Field Accelerator with Langmuir Probes", AIAA Journal, Vol. 12,No. 9. pp 1203-1209, September 1974

[16]S.L. Chen, T. Sekiguchi, "Instantaneous Direct Display System of Plasma Parameters by Means of Triple Probe", Journal of Appl. Phys., Vol. 36, No. 8, August 1965

[17]D.L. Tilley, A.J. Kelly, G.J. Jahn, "The Application of the Triple Probe Method to MPD Thruster Plumes",AIAA 90-2667, 21st IEPC, Orlando, FL, 1990

[18] M. Kanal, "Theory of Current Collection of Moving Cylindrical Probes", Journal of Appl. Phys., Vol. 35, No. 6, June 1964

[19] A.K. Jakubowski, "Effect of Angle of Incidence on the Response of Cylindrical Electrostatic Probes at Supersonic Speeds", AIAA Journal, Vol. 10, No. 8, August 1972

[20] G. Poisant, M. Dudeck, "Precise Velocity, Electron Temperature and Density Measurements with a Pulsed Langmuir Probe in a Rarefied Ionized Gas Flow", Rarefied gas dynamics, Vol. 14, 1984

[21] W.S. Gornall, "The World of Fabry-Perots", Lasers and Applications, July 1983

[22] W.L. Bohn, M.U. Beth, G. Nedder, "On Spectroscopic Measurements of Velocity Profiles and Non-equilibrium Radial Temperatures in an Argon Plasma Jet", J. Quant. Spectr. Radiat. Transf. Vol.7, pp 661-676, Pergamon press Ltd., 1967

[23] T.J. Pivirotto, W.D. Deininger, "Velocity Measurements in the Plume of an Arcjet Engine", AIAA 87-1063, 19th IEPC, Colorado Springs, CO 1987

[24] C.D. Scott, "Survey of Measurements of Flow Properties in Arc Jets", AIAA 5th Joint Thermoph. a. Heat Transf. Conf., Seattle, June 1990

[25] H.R. Griem, "Plasma Spectroscopy", McGraw-Hill, New York 1964.

[26] H.O. Schrade, Th. Wegmann, Th. Rösgen, "The Onset Phenomena explained by Run-away Joule heating", IEPC-91-022, 22nd IEPC, Viareggio, 1991

[27] H.J. Kaeppeler," Basic Equations and Elements of the Dispersion Relation for a Four-Fluid Formalism of Magneto-plasmadynamics with Non-Equilibrium Ionization", IEPC-91-059, 22nd IEPC, Viareggio, 1991

[28] A. Eberle:"Characteristic Flux Averaging Approach to the Solution of Euler's Equation", VKI lectures series, Computational fluid dynamics, 1987-04, 1987

[29] M. Auweter-Kurtz, H.L. Kurtz, H.O. Schrade, P.C. Sleziona," Numerical Modeling of the Flow Discharge in MPD-Thrusters", Journal of Propulsion and Power, Vol. 5, No. 1, pp 49 - 55, 1989

[30] P.C. Sleziona, M. Auweter-Kurtz, H.O. Schrade,"Numerical Evaluation of MPD Thrusters", IEPC 90-2602, 21st. IEPC, Orlando, Fl, 1990

[31] P.C. Sleziona et al.,"Non-Equilibrium Flow in an Arc Heated Wind Tunnel2, Workshop on Hypersonic Flows for Reentry Problems, Antibes, France, 1990

[32] P.C. Sleziona, M. Auweter-Kurtz, H.O. Schrade, Th. Wegmann,"Comparison of Numerical and Experimental Investigations of MPD Accelerators, AIAA-90-2663, 21st IEPC, Orlando, Fl, 1990

[33] H.O. Schrade, P.C. Sleziona,"Basic Processes of Plasma Propulsion", Interim Scientific Report, AFOSR Grant 86-0337, June 1990

[34] W. Finkelnburg, H. Maecker,"Elektrische Bögen und thermisches Plasma", Handbuch der Physik Bd. XXII, Gasentladungen II, Springer, Berlin, 1956

[35] M. Knoll et al. ,Gasentladungstabellen, Verlag von Julius Springer, Berlin, 1935

[36] A. Unsöld," Physik der Sternatmosphären", Springer, Berlin-Heidelberg-New York, 1986

[37] F. Maisenhälder and W. Mayerhofer," Jet-diagnostics of a Self-field Accelerator with Langmuir Probes", AIAA Journal, Vol. 12, No. 9, Sept. 1974, pp. 1203 - 1209

[38] F. Burhorn,"Berechnung und Messung der Wärmeleitfähigkeit von Stickstoff bis 13000°K", Zeitschrift für hysik 155, Erlangen, 1959